Non-reversible aging increases the solar absorptivity of African biomass burning plumes

Amie Dobracki[1*], Steven Howell[2], Pablo Saide[3], Steffen Freitag[2], Allison C. Aiken[4], Sharon Burton[5] Hugh Coe[6], Arthur J. Sedlacek III[7], Jonathan Taylor[6], HuihuiWu[6], Jens Redemann[8], Robert Wood[9], Paquita Zuidema[1*]

[1] University of Miami, Miami, Florida, USA

[2] University of Hawai`i at Mānoa, Honolulu, USA

[3] University of California Los Angeles, Los Angeles, California, USA

[4] Earth and Environmental Sciences Division, Los Alamos National Laboratory, Los Alamos, New Mexico, USA

[5]NASA Langley Research Center, Hampton, VA, USA

[6] Department of Earth and Environmental Sciences, University of Manchester, Manchester, UK

[7] Brookhaven National Laboratory, Upton, New York, USA

[8] University of Oklahoma, Norman, Oklahoma, USA

[9] University of Washington, Seattle, Washington, USA

Correspondence to: P. Zuidema (pzuidema@miami.edu) and A. Dobracki (amie.dobracki@rsmas.miami.edu)

Summary / Abstract

Biomass-burning emissions impact almost all of the radiative forcing terms considered by the IPCC, yet little is known about smoke aerosol aging in nature beyond a few days. The marine southeast Atlantic free-troposphere is a natural testbed for examining aging through photolysis/oxidation of African continental fire emissions advected westward. *In-situ* measurements primarily from September, 2016 indicate highly-oxidized aerosol with minimal primary source signatures after 4-9 model-predicted days since emission. Aerosol loses approximately one-half of its organic aerosol over the ocean. The organic aerosol to black carbon mass ratios decrease from 14 to 10, significantly lower than many model predictions. This mass loss, combined with stability in black carbon, supports an observed 20% increase in solar absorptivity. The decreased single scattering albedos, reaching 0.83 at 9 days, arguably represent the lowest values measured globally. The relationship of the aerosol properties to model-derived time since emission suggests a useful new modeling constraint.

Biomass burning, the largest source of carbon to the atmosphere globally, is fundamental to the Earth's global carbon cycle (Bowman et al., 2009; Bond et al., 2013). The emitted carbonaceous aerosols and trace gases include the greenhouse gases CO and CO_2, and significantly alter the atmospheric composition over large regions of the globe (Andreae, 2019). This in turn influences all of the gaseous, aerosol and aerosol-cloud interaction radiative forcing terms considered by the 5th IPCC Assessment (IPCC, 2013).

Despite the importance of biomass burning events on climate, how the properties of smoke change following long-range transport are still largely unknown. Smoke emissions undergoing long-range transport include the effluents from northern European and Russian forest fires reaching the Arctic basin (Cubison et al., 2011), wildfire smoke from western continental north America observed over Europe (Zheng et al., 2019; Baars et al., 2021), and aerosols from fires in southern Africa reaching south America (Holanda et al., 2020). Without wet or dry scavenging, the aerosol's areal coverage is increased through transport. As the carbonaceous aerosol-dominated plume is advected, it undergoes chemical, optical and physical changes. Although black carbon (BC) is released as a primary aerosol that is largely inert, the formation of secondary organic aerosol (SOA) provides additional mass in under two days through a condensation of gases, aqueous-phase chemistry (if sufficient moisture is available) and photochemistry (Jimenez et al., 2009). Further oxidation chemistry and photolysis can provide a subsequent SOA sink (Wagstrom et al., 2009; Cubison et al., 2011; Collier et al., 2016; Ahern et al., 2019; Cappa et al., 2020), prior to the aerosol's ultimate removal by deposition. Many global aerosol models overestimate OA concentrations in the remote free troposphere due to a lack of removal processes in the models (Heald et al., 2010; 2011; Spracklen et al., 2011; Tsigaridis et al., 2014; Hodzic et al., 2015; 2016; Shinozuka et al., 2020). More realistic model wet removal

rates (Cape et al., 2012; Katich et al., 2018; Lund et al., 2018; Hodzic et al., 2020) can only improve model realism when environmental conditions support convection. This implies additional loss mechanisms must be considered. In this study we only focus on non-aqueous-phase aging processes.

The free troposphere of the southeast Atlantic is a natural testbed for understanding SOA aging processes focused on photolysis and oxidation in the absence of aqueous-phase chemistry. Southern Africa produces approximately one-third of the world's fire-emitted carbon (van der Werf et al., 2010). The prevailing meteorology, by advecting the smoke westward over the ocean, can provide a simplified environment in which to isolate those biomass-burning aerosol (BBA) characteristics stemming from photolytic/oxidation aging. Recent results already highlight that aerosol properties from this region are unusual for being highly absorbing of sunlight (Zuidema et al., 2018; Chylek et al., 2019; Pistone et al., 2019; Holanda et al., 2020; Taylor et al. 2020; Denjean et al., 2020; Mallet et al., 2020; Shinozuka et al., 2020). This is important for climate because the global maximum of absorbing aerosol above cloud occurs here (Waquet et al., 2013), providing a distinct radiative warming over the region (Doherty et al., 2021). While climate models discern an ensemble-mean direct radiative warming, individual models disagree strongly on magnitude and even sign (Myrhe et al, 2013; Zuidema et al., 2016; Haywood et al., 2021). Aerosol aging processes are becoming better articulated within global models (Shrivastava et al., 2019; Konovalov et al., 2020; Hodzic et al., 2020; Wang et al., 2020; Lou et al., 2020), but the ones that focus on biomass burning primarily draw support from Northern Hemisphere *in-situ* observations (Jimenez et al., 2009; Garofalo et al., 2019; Adachi et al., 2019; Kleinman et al., 2020; Schill et al., 2020). More recent assessments (Lund et al., 2018; Schill et al., 2020; Hodzic et al., 2020; Brown et al., 2021) include the southeast Atlantic (SEA)

within their global analyses, but do not focus on the SEA region or on the impacts of BB aging greater than a week important for global long-range transport.

Datasets and approach

The *in-situ* smoke aerosol composition and optical property observations are drawn from 6 flights of the NASA Earth Venture Suborbital-2 ORACLES (ObseRvations of Aerosols above CLouds and their intEractionS; Redemann et al., 2021) aircraft deployments, occurring primarily in September, 2016. These flights were selected because backtrajectories suggest similar source regions and because at least 20 minutes of OA>20 ug m^{-3} data are available from each flight, reducing the absolute (relative) uncertainty to at most 1.6 ug m^{-3} (8%). The flight tracks are shown relative to the satellite-derived above-cloud aerosol optical depths in Fig. S1, and Fig. S2 depicts the individual flight tracks and the aerosol forecasts, with the Methods containing a fuller description of the flight selection protocol. The fire sources are primarily miombo woodland savanna grasses and agricultural fields (Shea et al., 1996; Christian et al., 2003; Vakkari et al., 2008). Sources of urban pollution are few, and modified combustion efficiency values (>0.97; Fig. S3) indicate flame-efficient fires (Collier et al., 2016; Zhou et al., 2017). Aqueous-phase oxidation is excluded by only examining aerosol from altitudes above 1.5 km with relative humidities (RH) < 80%. Dilution, by which OA evaporates through mixing with cleaner environmental air, is controlled by selecting when OA:BC ratios become stable with OA mass (Fig. S4). BC to carbon monoxide ratios vary within 30% for each flight, with a maximum of 12.2 ± 1.1 on 4 September and a minimum of 8.9 ± 1.4 ng m^{-3} ppb^{-1} on 24 September (Fig. S5). A statistically-insignificant decrease over the 2016 BB season is hinted at. Eck et al., (2013) suggest the most combustible fuel may be ignited earlier in the BB season.

An aerosol mean atmospheric age is estimated using CO emissions tracers released daily at the fire sources within the ORACLES aerosol forecast model: the Weather Research Forecasting model configured with Aerosol Aware Microphysics (Saide et al., 2016). The current analysis takes advantage of the model's prior use for seeking out the smoke layers that are subsequently sampled by the aircraft. For these thicker aerosol layers, the model-derived days since emission are almost always greater than four days. Measurements of *f44*, the fraction of the OA mass spectrum signal at *m/z 44* relative to the total OA mass concentration, indicate independent chemical aging based on aerosol mass spectrometry (Canagaratna et al., 2015) and correlate well with the model-derived age estimates (Fig. S5). Mean *f44* values exceed 0.20 after 4 days, almost on par with f44 values from Asian/Siberian smoke transported to Alaska over two weeks (Fig. S6; Cubison et al., 2011). The high *f44* values are consistent with highly oxidized aerosol (Fig. S6): average plume values of the hydrogen-to-carbon ratio (H:C), oxygen-to-carbon ratio (O:C), and organic-aerosol-to-organic-carbon ratio (OA:OC) are 1.2 ± 0.1, 0.7 ± 0.1, and 2.2 ± 0.1, respectively (Canagaratna et al., 2015). These values indicate a mixture of (aged) low- and semi-volatile oxygenated OA (Jimenez et al., 2009; Huffman et al., 2009; Hodzic et al., 2020).

Organic aerosol loss and radiative implications

The mean submicron mass fractions of the six flights combined are 66% OA, 10% nitrate (NO_3), 11% sulfate (SO_4), 5% ammonium (NH_4), and 8% BC. The organic aerosol, nitrate, and ammonium masses decrease after 4 days, with most of the mass loss occurring by day 7 and stabilizing thereafter (Figs. 1a-c). The OA:OC ratio (Fig. 1d), a robust measure of the oxygen content useful for model evaluation (Hodzic et al., 2020; Luo et al, 2020), increases until day 7, indicating continued processing of the organics, remaining stable thereafter. SO_4:BC remains

92 constant at approximately 1.6-1.7 (not shown), indicating its formation as a secondary inorganic
93 aerosol has ended. The O:C ratios increase slightly, indicating continuing oxidation (Kroll and
94 Seinfeld, 2008), if slight (Fig. S7). The chemical compositions for the same aerosol age differ
95 between flights (Figs. S8-S9). OA:BC ratios at aerosol ages of 7-8 days range from a mean of
96 8.7 ug m^{-3} on 31 August, 2017 to 13.2 ug m^{-3} on 25 September, 2016 (Fig. S8). Aerosol aged 5-
97 6 days has a similar range (means of 8.9 ug m^{-3} on 31 August 2017 to 13.8 ug m^{-3} on 6
98 September, 2016). The different OA:BC ratios for similarly-aged air masses from similar source
99 regions may reflect remaining differences in the (unmeasured) emitted volatile organic
100 compounds (Ahern et al., 2009; McFiggans et al., 2019). Yet, with the exception of the flight on
101 25 September, 2016, a decrease in OA:BC with age is evident on the other 5 flights (Fig. S8).
102 The reduction is particularly noticeable in the flight with the majority of the youngest (4-5 days
103 in age) aerosol. This flight was conducted on 24 September, 2016 with the express goal of
104 sampling a plume of younger, dense aerosol plume as close to its source as possible while still
105 over international waters (Fig. S2b).
106 The loss of aerosol with age has implications for the single scattering albedo (SSA, the
107 sunlight scattering/(scattering+absorption) ratio per particle). As the aerosol mass decreases with
108 age while the BC mass remains relatively constant, the smoke aerosol absorbs more sunlight per
109 particle. The SSA, calculated at 530 nm wavelength (see Methods), decreases from a mean value
110 of 0.86 at an aerosol age of 4-5 days to 0.83 at an aerosol age of 8-9 days (Fig. 1e), an
111 approximate 20% increase in absorptivity per particle (the co-albedo, or 1-SSA). The BC mass
112 fraction increases from 4% to 10% over this time span. The increase in co-albedo can increase
113 the direct aerosol radiative effect over a broad region by ~ +1 W m^{-2} (Mallet et al., 2020), and
114 generates an uncertainty in retrieved above-cloud aerosol optical depth of approximately 40%

115 (Meyer et al., 2015). The [0.87,0.91] values applied within Meyer et al., (2015) indicate a lack of
116 prior anticipation of the low SSA values. Sulfate, which possesses an SSA of 1, contributes a
117 mass fraction approximately one-half that measured in many northern hemisphere campaigns
118 (Jimenez et al, 2009). The low sulfate fraction may also contribute to the high particle
119 absorptivity.

120 Fig. 1 provides the perspective in which different air masses containing aerosol of
121 different ages are aggregated together from all flights. Data from one flight, 9/25/2016, indicates
122 an increase in OA:BC between an age of 6-7 days to 7-8 days, in contrast to the other 5 flights
123 (Fig. S7). This contribution explains a slight rise evident at 7-8 days in Fig. 1. The prior flight
124 on 9/24/2016 provides a semi-Lagrangian perspective on aerosol aging. The 9/24/2016 flight
125 flew close to the Namibian/Angola border (Fig. S2 and S3b) for the express purpose of sampling
126 slightly fresher aerosol within the strong zonal winds comprising the African Easterly Jet-South
127 (AEJ-S; Adebiyi and Zuidema, 2016; Ryoo et al., 2021). The *in-situ* sampling on 9/24/2016
128 included a long level leg and 4 vertical profiles, and maps well upon a lidar altitude-latitude
129 curtain of the aerosol backscatter coefficient measured during an overflight coinciding with the
130 lower plane at 11^0E, 10^0S (Fig. 2a). Although the aerosol sampled further offshore on 9/25/2016
131 was beyond that of smoke advected west from profile 3 on 9/24 (Fig. 2b), the similar vertical
132 wind structure on 9/25 (Fig. 2c; the AEJ-S is demarcated by westward wind speeds > 6 m s^{-1} and
133 is stronger further north), indicates the same transport pattern dominated. Small differences in
134 the oxidation O:C and H:C ratios between the two flights either indicate small differences in
135 burning conditions (Ng et al., 2011), or, fresher aerosol that is taking longer to oxidize within a
136 larger mass concentration (Lambe et al., 2012). Yet, OA:BC decreases between the two days,

nevertheless (Fig. 2d). A slight increase in H:C and OA:OC and slight decrease on O:C between the two days provides further detail on the chemical aging of the oxygenated aerosol (Fig. 2e-f).

Reversible versus irreversible aging

Nitrate only contributes 10% to the total sampled free-tropospheric aerosol mass, but an examination of its thermodynamical partitioning (a reversible gas->particle phase transition favored at lower temperatures/higher humidities; Nenes et al., 1997) illuminates how prevailing circulation patterns over the southeast Atlantic enable OA mass loss to photolysis/oxidation. We apply the approach of Farmer et al., (2010) to estimate the inorganic nitrate (IN, primarily NH_4NO_3) fraction (see Methods), keeping in mind that it is an indirect inference, and begin with two illustrative cases (Fig. 3; locations indicated on Fig. S1).

The 24 September, 2016 profile at 12.3˚S, 11˚E (Fig. 3a; southernmost profile on Fig. 2a) occurred slightly south of the AEJ-S core. The upper-altitude winds also transport moisture (Fig. S9), consistent with climatological expectations (Adebiyi et al., 2015; Pistone et al., 2019), generating relative humidities exceeding 80% above 4 km combined with the cooler high-altitude temperatures (Fig. 3a). The water vapor mixing ratio and statically-stable potential temperature profiles (Fig. S10a) indicate little mixing of air between different altitudes. The 9/24 profile is broadly comprised of one main aerosol layer centered on 5 km of ~4 days in age, and a slightly older smoke layer of ~5 days in age, centered on 3 km (Fig. 3b).

The 8/31/2016 profile further south (16.4˚S, 6.5˚E) sampled mildly eastward winds (0-5 m/s) between 2.5-5.5 km (Fig. 3b) associated with an impinging mid-latitude disturbance (Ryoo et al., 2021). Synoptically-driven ascent (Diamond et al., 2018) mixes moisture upward (Fig. S9c), generating a linear increase in RH with height (Fig. 3c) that reaches 80% and is capable of generating mid-level clouds elsewhere (Adebiyi et al., 2020). The aerosol is older, at

160 approximately 9 days in age above 3.5 km, and, in this case, overlies aerosol aged between 5-6
161 days below 3 km (Fig. 3d).

162 The NO_3:BC and OA:BC ratios increase with altitude for both profiles. The lower
163 temperatures and high relative humidities above 4 km favor a reversible partitioning of the
164 inorganic nitrate (IN) to the particle phase (Nenes et al., 1997; Zhang et al., 1999) mildly evident
165 in increases of ~0.05 within both IN:NO_3 profiles. A similar argument applies to semi-volatile
166 OA (Donahue et al., 2006; Robinson et al., 2007; Koop et al., 2011; Shiraiwa et al., 2011;
167 Donahue et al., 2012). The more dominant signal is an increase in the mean IN fraction from
168 ~0.20 to ~0.25 for the older aerosol on 8/31/2016 compared to 9/24/2016. Though this could also
169 reflect smoke emissions that contain more inorganic nitrate initially on 8/31/2016 compared to
170 9/24/2016, the difference between the two days is also consistent with a loss of organic nitrate
171 with age.

172 A compositing of OA:BC, NO_3:BC and aerosol age by RH reveals a relationship
173 common to many of the ORACLES September flights, in which younger aerosol occupies more
174 humid environments than does older aerosol (Fig. 4b). The mean NO_3:BC ratio decreases by
175 almost 50% as the RH decreases from ~70% to ~10% (Fig. 4a), consistent with a thermodynamic
176 repartitioning, but also with organic nitrate loss through photolysis/oxidation as the mean aerosol
177 age increases. The coassociation can be understood through a slow large-scale subsidence acting
178 on aerosol-laden air. The mean OA:BC ratio decrease from 8.86 for RH values between 40-60%
179 to 8.06 for RH < 20%. This indicates that a thermodynamical repartition can only explain a
180 relative decrease in OA:BC with age of 10% at best. We conclude that most OA loss in the
181 southeast Atlantic free troposphere is irreversibly lost through either photolytics or oxidation
182 after 4 days, with thermodynamic repartitioning providing a minor contribution (dilution and wet

183 removal processes already excluded by construction). While this finding is not new in
184 qualitative terms (e.g., Capes et al., 2008; Jolleys et al., 2015; Hodzic et al., 2015; Konovalov et
185 al., 2019), the abundance of data combined with the model age estimates provide an original
186 observationally-based quantification of the OA mass loss (Fig. 1).

187 **Photolysis/oxidation process Assessment**

188 Modeled SOA lifetimes are sensitive to the branching ratio between functional groups
189 added to lengthen the carbon chain, and fragmentation, in which carbon-carbon bonds are broken
190 during oxidation, shortening the carbon chain length and allowing the oxidized organic aerosol to
191 become more volatile (George et al., 2010; Kroll et al., 2011; Kroll et al., 2015; Shrivastava et
192 al., 2015; Hodshire et al., 2019). Oligomerization , in which condensed phase gases increase the
193 particle aerosol concentration, can also affect the SOA lifetime (Donahue et al., 2006). The loss
194 of organic aerosol over time above the southeast Atlantic, along with increasing oxidation, is
195 more consistent with fragmentation. Absorption angstrom exponent (AAE) values suggest a lack
196 of brown carbon, with mean AAE values of 1.1-1.2 over the 470-660 nm wavelength range
197 stabilizing after 7 days (Fig. S11); extrapolation indicates absorption of ultraviolet light is also
198 low (Taylor et al., 2020). A wavelength-independent SOA loss mechanism is not entirely
199 congruent with fragmentation, and the convergence of OA characteristics after a week to values
200 of OA:BC < 11 (Fig. 1 and Fig. S8) suggests a balance must be occurring between
201 heterogeneous oxidation loss and chromophere production through photolysis and/or nitrogen
202 chemistry (O'Brien and Kroll, 2019). Overall, Fig. 1 supports the aging model of Jimenez et al.,
203 (2009), in which the original source signature of smoke becomes replaced with that of
204 atmospheric oxidation. Consistent with this, a separate analysis finds more oxidized aerosol and

205 little remaining organic nitrate by the time the smoke aerosol arrives at Ascension Island further
206 west a 14.5^0W (Wu et al., 2020).

207 Lensing, by which absorption increases through a Mie effect generated by the OA
208 coating, is in theory able to both decrease the SSA and maintain a constant AAE (Lack et al.,
209 2012; Cappa et al., 2012). Mie calculations, which require spherical shapes, may overestimate
210 lensing effects, but aged BBA do compact from the fractals that can define soot upon emission
211 (Taylor et al., 2020). There is some indication that the co-emitted sulfate can contribute to the
212 lensing (Christian et al., 2003), and combined with other absorptive coating characteristics
213 (Denjean et al., 2020) and photo-bleaching (Taylor et al., 2020), this can explain why the BBA
214 over the remote southeast Atlantic is more light-absorbing than noted elsewhere.

215 In sum, the relatively simple aerosol environment of the southeast Atlantic free
216 troposphere can support a unique focus on natural photolytic/oxidative aging, isolated from the
217 other processes affecting BBA composition. Measurements selected with that in mind and
218 combined with quantitative age estimates provide a new modeling constraint for the
219 representations of BBA in global aerosol models with increasingly sophisticated SOA schemes
220 (e.g., Lou et al., 2020). This study adds to literature indicating that OA model estimates made by
221 multiplying the organic carbon by a factor of 1.4 will underestimate OA in this (and other)
222 regions (Aiken et al., 2008; Shinozuka et al., 2020; Doherty et al., 2021). Modeled OA:BC ratios
223 can also be overestimated by over a factor of two over the southeast Atlantic in global models
224 with sophisticated aerosol schemes (Chylek et al., 2019), suggesting the loss of OA with aging or
225 slower SOA production processes (Kroll and Seinfeld, 2008; McFiggans et al., 2009), or the
226 emission factors at the source, may still not be well-accounted for.

227
228 **Data Availability**

The data are available through doi:10.5067/Suborbital/ORACLES/P3/2016_V2 and doi: 10.5067/Suborbital/ORACLES/P3/2017_V2

Acknowledgements

ORACLES is a NASA Earth Venture Suborbital-2 investigation, funded by the US National Aeronautics and Space Administration (NASA)'s Earth Science Division and managed through the Earth System Science Pathfinder Program Office (grant no. NNH13ZDA001N-EVS2). This work was further supported by the US Department of Energy (DOE: grant DE-SC0018272 to P.Z. and P.S. and DE-SC0021250 to P.Z.).

Author Contributions

The present work was conceived by S.H., P.S., P.Z. and A.D. S.F. contributed to the HiGEAR data analysis, A.S. provided the BC datasets and P.S. the WRF-AAM model age estimates. Portions of this work first appeared in the M.S. thesis of A.D at U. of Hawaii. All authors contributed to the final writing.

Additional information

The authors declare no competing financial interests.

References

Main Text

Adebiyi, A. A., Zuidema, P., & Abel, S. J. The Convolution of Dynamics and Moisture with the Presence of Shortwave Absorbing Aerosols over the Southeast Atlantic. *J. Clim.,* **28**, 1997-2024, doi:10.1175/jcli-d-14-00352.1 (2015).

Adebiyi, A. A. & Zuidema, P. The role of the southern African easterly jet in modifying the southeast Atlantic aerosol and cloud environments. *Quart J. Royal Meteor. Soc.,* **142**, 1574-1589, doi:10.1002/qj.2765 (2016).

Adebiyi, A. A., Zuidema, P., Chang, I., Burton, S. P. & Cairns, B. Mid-level clouds are frequent above the southeast Atlantic stratocumulus clouds. *Atmos. Chem. Phys.,* **20**, 11025-11043, doi:10.5194/acp-20-11025-2020 (2020).

Adachi, K., et al., Spherical tarball particles form through rapid chemical and physical changes of organic matter in biomass-burning smoke. *PNAS*, **116,** 19336-19341, doi:10.1073/pnsa.1900129116. (2019)

Ahern, A. T., Robinson, E. S., Tkacik, D. S., Saleh, R., Hatch, L. E., Barsanti, K. C., et al. Production of secondary organic aerosol during aging of biomass burning smoke from fresh fuels and its relationship to VOC precursors. *J. Geophys. Res.*, **124**, 3583– 3606. doi:10.1029/2018JD029068

Aiken, A. C. *et al.* O/C and OM/OC ratios of primary, secondary, and ambient organic aerosols with high-resolution time-of-flight aerosol mass spectrometry. *Environ Sci Technol* **42**, 4478-4485 (2008).

Andreae, M. O. Emission of trace gases and aerosols from biomass burning – an updated assessment. *Atmos. Chem. Phys.,***19**, 8523-8546, doi:10.5194/acp-19-8523-2019 (2019).

Baars, H., Radenz, M., Floutsi, A. A., Engelmann, R., Althausen, D., Heese, B., et al. (2021). Californian wildfire smoke over Europe: A first example of the aerosol observing capabilities of Aeolus compared to ground-based lidar. *Geophy. Res. Lett.*, **48**, e2020GL092194. doi:10.1029/2020GL092194.

Bond, T. C. *et al.* Bounding the role of black carbon in the climate system: A scientific assessment. *J. Geophys. Res.,* **118**, 5380-5552, doi:10.1002/jgrd.50171 (2013).

Bowman, D. M. J. S. *et al.* Fire in the Earth System. *Science* **324**, 481-484, doi:10.1126/science.1163886 (2009).

Brown, H., Liu, X., Pokhrel, R. *et al.* Biomass burning aerosols in most climate models are too absorbing. *Nat Commun* **12,** 277 doi:10.1038/s41467-020-20482-9 (2021)

Canagaratna, M. R., Jimenez, J. L., Kroll, J. H., *et al*.. Elemental ratio measurements of organic compounds using aerosol mass spectrometry: characterization, improved calibration, and implications, *Atmos. Chem. Phys.*, **15**, 253–272, doi: 10.5194/acp-15-253-2015, (2015)

Cape, J. N., Coyle, M. & Dumitrean, P. The atmospheric lifetime of black carbon. *Atmos. Env.,* **59**, 256-263, doi:10.1016/j.atmosenv.2012.05.030 (2012).

Capes, G. *et al.* Aging of biomass burning aerosols over West Africa: Aircraft measurements of chemical composition, microphysical properties, and emission ratios. *J. Geophys. Res.,***113**, doi:10.1029/2008jd009845 (2008).

Cappa, C. D., Onasch, T. B., Massoli, P., Worsnop, D., Bates, T. S., Cross, E., Davidovits, P., Hakala, J., Hayden, K., Jobson, B. T., Kolesar, K. R., Lack, D. A., Lerner, B., Li, S. M., Mellon, D., Nuaanman, I., Olfert, J., Petaja, T., Quinn, P. K., Song, C., Subramanian, R., Williams, E. J., and Zaveri, R. A.: Radiative absorption enhancements due to the mixing state of atmospheric black carbon, Science, 337, 1078–1081, https://doi.org/10.1126/science.1223447, 2012.

Cappa, C. D. *et al.* Biomass-burning-derived particles from a wide variety of fuels – Part 2: Effects of photochemical aging on particle optical and chemical properties. *Atmospheric Chemistry and Physics* **20**, 8511-8532, doi:10.5194/acp-20-8511-2020 (2020).

Christian, T. J., B. Kleiss, R. J. Yokelson, R. Holzinger, P. J. Crutzen, W. M. Hao, B. H. Saharjo, and D. E. Ward, Comprehensive laboratory measurements of biomass-burning emissions: 1. Emissions from Indonesian, African, and other fuels, *J. Geophys. Res*., **108**(D23), 4719, doi:10.1029/2003JD003704, 2003

Chylek, P. *et al.* Mie Scattering Captures Observed Optical Properties of Ambient Biomass Burning Plumes Assuming Uniform Black, Brown, and Organic Carbon Mixtures. *J. Geophys. Res.,* **124**, 11406-11427, doi:10.1029/2019jd031224 (2019).

Collier, S. *et al.* Regional Influence of Aerosol Emissions from Wildfires Driven by Combustion Efficiency: Insights from the BBOP Campaign. *Environ Sci Technol* **50**, 8613-8622, doi:10.1021/acs.est.6b01617 (2016)

Cubison, M. J. *et al.* Effects of aging on organic aerosol from open biomass burning smoke in aircraft and laboratory studies. *Atmos. Chem. Phys.,* **11**, 12049-12064, doi:10.5194/acp-11-12049-2011 (2011).

Denjean, C. *et al.* Unexpected Biomass Burning Aerosol Absorption Enhancement Explained by Black Carbon Mixing State. *Geophysical Research Letters* **47**, doi:10.1029/2020gl089055 (2020).

Diamond, M. S. *et al*. Time-dependent entrainment of smoke presents an observational challenge for assessing aerosol– cloud interactions over the southeast Atlantic Ocean, *Atmos. Chem. Phys.*, **18**, 14623–14636, doi:10.5194/acp-18-14623-2018, (2018).

Doherty, S. J., Saide, P. E., Zuidema, P., Shinozuka, Y., Ferrada, G. A., Gordon, H., *et al.*, Modeled and observed properties related to the direct aerosol radiative effect of biomass burning aerosol over the Southeast Atlantic, *Atmos. Chem. Phys. Discuss*. doi:10.5194/acp-2021-333, (2021).

Donahue NM, Robinson AL, Stanier CO, Pandis SN. Coupled partitioning, dilution, and chemical aging of semivolatile organics. *Environ Sci Technol*., **40**, p.2635-43. doi: 10.1021/es052297c. (2006)

Donahue, N. M., Kroll, J. H., Pandis, S. N. & Robinson, A. L. A two-dimensional volatility basis set – Part 2: Diagnostics of organic-aerosol evolution. *Atmos. Chem. Phys.,* **12**, 615-634, doi:10.5194/acpd-12-615-2012 (2012).

Eck, T. F., B. N. Holben, J. S. Reid, M. M. Mukelabai, S. J. Piketh, O. Torres et al. A seasonal trend of single scattering albedo in southern African biomass-burning particles: Implications for satellite products and estimates of emissions for the world's largest biomass-burning source, *J. Geophys. Res.*, **118**, doi:10.1002/jgrd.50500 (2013).

Farmer, D. K. *et al.* Response of an aerosol mass spectrometer to organonitrates and organosulfates and implications for atmospheric chemistry. *Proc Natl Acad Sci U S A* **107**, 6670-6675, doi:10.1073/pnas.0912340107 (2010).

Garofalo, L. A., Pothier, M. A., Levin, E. J. T., Campos, T., Kreidenweis, S. M., and Farmer, D. K.: Emission and Evolution of Submicron Organic Aerosol in Smoke from Wildfires in the Western United States, *ACS Earth Space Chem.,* **3**, 1237–1247, doi:10.1021/acsearthspacechem.9b00125, (2019)

George, I. J. & Abbatt, J. P. D. Chemical evolution of secondary organic aerosol from OH-initiated heterogeneous oxidation. *Atmos. Chem. Phys.,* **10**, 5551-5563, doi:10.5194/acp-10-5551-2010 (2010).

Haywood, J. M. *et al.* Overview: The CLoud-Aerosol-Radiation Interaction and Forcing: Year-2017 (CLARIFY-2017) measurement campaign. *Atmos. Chem. Phys.,* **21**, p. 1049-1084. doi:10.5194/acp-21-1049-2021 (2021).

Heald, C. L. *et al.* Exploring the vertical profile of atmospheric organic aerosol: comparing 17 aircraft field campaigns with a global model. *Atmos. Chem. Phys.,* **11**, 12673-12696, doi:10.5194/acp-11-12673-2011 (2011).

Heald, C. L. *et al.* A simplified description of the evolution of organic aerosol composition in the atmosphere. *Geophys. Res. Lett.* **37**, doi:10.1029/2010gl042737 (2010).

Hodshire, A. L. *et al.* Aging Effects on Biomass Burning Aerosol Mass and Composition: A Critical Review of Field and Laboratory Studies. *Environ Sci Technol* **53**, 10007-10022, doi:10.1021/acs.est.9b02588 (2019).

Hodzic, A. *et al.* Organic photolysis reactions in tropospheric aerosols: effect on secondary organic aerosol formation and lifetime. *Atmos. Chem. Phys.,* **15**, 9253-9269, doi:10.5194/acp-15-9253-2015 (2015).

Hodzic, A., *et al.* Rethinking the global secondary organic aerosol (SOA) budget: stronger production, faster removal, shorter lifetime. *Atmos. Chem. Phys*., **16**, 7917-7941, doi:10.5194/acp-16-7917-2016 (2016).

Hodzic, A. *et al.* Characterization of organic aerosol across the global remote troposphere: a comparison of ATom measurements and global chemistry models. *Atmos. Chem. Phys.,* **20**, 4607-4635, doi:10.5194/acp-20-4607-2020 (2020).

Holanda, B. A. *et al.* Influx of African biomass burning aerosol during the Amazonian dry season through layered transatlantic transport of black carbon-rich smoke. *Atmos. Chem. Phys.***20**, 4757-4785, doi:10.5194/acp-20-4757-2020 (2020).

Huffman, J. A., et al., Chemically-resolved volatility measurements of organic aerosol from different sources, *Environ. Sci. Technol.* 2009, 43, 14, 5351–5357, doi:10.1021/es803539d (2009)

IPCC, 2013: Climate Change 2013: Working Group I Contribution to the Fifth Assessment Report of the Intergovernmental Panel on Climate Change. 1535 (Cambridge University Press, Cambridge, United Kingdom and New York, USA, 2013).

Jimenez, J. L. *et al.* Evolution of organic aerosols in the atmosphere. *Science* **326**, 1525-1529, *Science*, doi:10.1126/science.1180353 (2009).
Jolleys, M. D. *et al.* Properties and evolution of biomass burning organic aerosol from Canadian boreal forest fires. *Atmos. Chem. Phys.,* **15**, 3077-3095, doi:10.5194/acp-15-3077-2015 (2015)
Katich, J. M. *et al.* Strong Contrast in Remote Black Carbon Aerosol Loadings Between the Atlantic and Pacific Basins. *J. Geophys. Res.,* **123**, doi:10.1029/2018jd029206 (2018).
Kleinman, L. I., Sedlacek III, A. J., Adachi, K., Buseck, P. R., Collier, S., *et al.* Rapid evolution of aerosol particles and their optical properties downwind of wildfires in the western US, *Atmos. Chem. Phys.,* **20**, 13319–13341, doi:10.5194/acp-20-13319-2020, (2020).
Konovalov, I. B., Beekmann, M., Golovushkin, N. A. & Andreae, M. O. Nonlinear behavior of organic aerosol in biomass burning plumes: a microphysical model analysis. *Atmos. Chem. Phys.* **19**, 12091-12119, doi:10.5194/acp-19-12091-2019 (2019).
Koop, T., Bookhold, J., Shiraiwa, M. & Poschl, U. Glass transition and phase state of organic compounds: dependency on molecular properties and implications for secondary organic aerosols in the atmosphere. *Phys Chem Chem Phys* **13**, 19238-19255, doi:10.1039/c1cp22617g (2011).
Kroll, J. H. and J. H. Seinfeld. Chemistry of secondary organic aerosol: Formation and evolution of low-volatility organics in the atmosphere; *Atmos. Env.* **42,** 3593-3624 (2008)
Kroll, J. H. *et al.* Carbon oxidation state as a metric for describing the chemistry of atmospheric organic aerosol. *Nat Chem* **3**, 133-139, doi:10.1038/nchem.948 (2011).
Lack, D. A., Langridge, J., Bahreni, R., Cappa, C. D., Middlebrook, A., and Schwarz, J. P.: Brown Carbon and Internal Mixing in Biomass Burning Particles, *P. Natl. Acad. Sci*. USA, 10, 14802–14807, https://doi.org/10.1073/pnas.1206575109, 2012.
Lambe, A. T.; Onasch, T. B.; Croasdale, D. R.; Wright, J. P.; Martin, A. T.; Franklin, J. P.; Massoli, P.; Kroll, J. H.; Canagaratna, M. R.; Brune, W. H.; Worsnop, D. R.; Davidovits, P. Transitions from Functionalization to Fragmentation Reactions of Laboratory Secondary Organic Aerosol (SOA) Generated from the OH Oxidation of Alkane Precursors *Environ. Sci. Technol.* 46 (10) 5430–5437 DOI: 10.1021/es300274t (2012)
Lou, S. *et al.* New SOA Treatments Within the Energy Exascale Earth System Model (E3SM): Strong Production and Sinks Govern Atmospheric SOA Distributions and Radiative Forcing. *J. Adv. Mod. Earth Sys.* **12**, doi:10.1029/2020ms002266 (2020).
Lund, M. T. *et al.* Short Black Carbon lifetime inferred from a global set of aircraft observations. *npj Clim.Atmos. Sci.,* **1**, doi:10.1038/s41612-018-0040-x (2018).
Mallet, M. *et al.* Direct and semi-direct radiative forcing of biomass-burning aerosols over the southeast Atlantic (SEA) and its sensitivity to absorbing properties: a regional climate modeling study. *Atmos. Chem. Phys.* **20**, 13191-13216, doi:10.5194/acp-20-13191-2020 (2020).
May, A. A. *et al.* Observations and analysis of organic aerosol evolution in some prescribed fire smoke plumes. *Atmos. Chem. Phys.* **15**, 6323-6335, doi:10.5194/acp-15-6323-2015 (2015).
McFiggans, G., Mentel, T.F., Wildt, J. *et al.* Secondary organic aerosol reduced by mixture of atmospheric vapours. *Nature* **565,** 587–593 doi: 10.1038/s41586-018-0871-y (2019)
Meyer, K., Platnick, S. & Zhang, Z. Simultaneously inferring above-cloud absorbing aerosol optical thickness and underlying liquid phase cloud optical and microphysical properties using MODIS. *J. Geophys. Res.* **120**, 5524-5547, doi:10.1002/2015jd023128 (2015).
Myhre, G. Consistency Between Satellite-Derived and Modeled Estimates of the Direct Aerosol Effect. *Science* **325**, 187-190, doi:10.1126/science.1174461 (2009).
Nenes, A., Pandis, S. N. & Pilinis, C. ISORROPIA: A New Thermodynamic Equilibrium Model for Multiphase Multicomponent Inorganic Aerosols. *Aquatic Geochemistry* **4**, 123-152 (1997).
Ng, N. L., Canagaratna, M. R., Zhang, Q., Jimenez, J. L., Tian, J., Ulbrich, *et al.*,: Organic aerosol components observed in Northern Hemispheric datasets from Aerosol Mass Spectrometry, *Atmos. Chem. Phys.*, 10, 4625–4641, doi:10.5194/acp-10-4625-2010, (2010)

O'Brien, R. E. & Kroll, J. H. Photolytic Aging of Secondary Organic Aerosol: Evidence for a Substantial Photo-Recalcitrant Fraction. *J Phys Chem Lett* **10**, 4003-4009, doi:10.1021/acs.jpclett.9b01417 (2019).

Pistone, K. *et al.* Intercomparison of biomass burning aerosol optical properties from in situ and remote-sensing instruments in ORACLES-2016. *Atmos, Chem. Phys.***19**, 9181-9208, doi:10.5194/acp-19-9181-2019 (2019).

Robinson, A. L., *et. al.,* Rethinking organic aerosols: semivolatile emissions and photochemical aging. *Science*, **315**, 1259, doi:10.1126/science.1133061 (2007).

Ryoo, J.-M., Pfister, L., Ueyama, R., Zuidema, P., Wood, R., Chang, I., and Redemann, J.: A meteorological overview of the ORACLES (ObseRvations of Aerosols above CLouds and their intEractionS) campaign over the southeast Atlantic during 2016–2018, *Atmos. Chem. Phys. Discuss*. [preprint], https://doi.org/10.5194/acp-2021-274, in review, 2021.

Saide, P. E. *et al.* Assessment of biomass burning smoke influence on environmental conditions for multi-year tornado outbreaks by combining aerosol-aware microphysics and fire emission constraints. *J Geophys. Res.* **121**, 10294-10311, doi:10.1002/2016JD025056 (2016).

Schill, G. P. *et al.* Widespread biomass burning smoke throughout the remote troposphere. *Nature Geo.* **13**, 422-427, doi:10.1038/s41561-020-0586-1 (2020).

Shea, R. W., B. W. Shea, J. B. Kauffman, D. E. Ward, C. I. Haskins, and M. C. Scholes, Fuel biomass and combustion factors associated with fires in savanna ecosystems of South Africa and Zambia, *J. Geophys. Res*., 101, 23,551– 23,568, 1996

Shinozuka, Y., *et al.* Modeling the smoky troposphere of the southeast Atlantic: a comparison to ORACLES airborne observations from September of 2016. *Atmos. Chem. Phys.*, **20**, p. 11,491-11,526, doi:10.5194/acp-20-11491-2020 (2020)

Shiraiwa, M., Ammann, M., Koop, T. & Poschl, U. Gas uptake and chemical aging of semisolid organic aerosol particles. *Proc Natl Acad Sci U S A* **108**, 11003-11008, doi:10.1073/pnas.1103045108 (2011).

Shrivastava, M., *et al.*, Global transformation and fate of SOA: Implications of low-volatility SOA and gas-phase fragmentation reactions. *J. Geophys. Res.*, **120**, 4169–4195. doi: 10.1002/2014JD022563 (2015

Shrivastava, M., et al. Recent advances in understanding secondary organic aerosol: Implications for global climate forcing, *Rev. Geophys.*, **55** 509–559, doi:10.1002/2016RG000540 (2017)_

Spracklen, D. V. *et al.* Aerosol mass spectrometer constraint on the global secondary organic aerosol budget. *Atmos. Chem. Phys.* **11**, 12109-12136, doi:10.5194/acp-11-12109-2011 (2011).

Taylor, J. W. *et al.* Absorption closure in highly aged biomass burning smoke. *Atmospheric Chemistry and Physics* **20**, 11201-11221, doi:10.5194/acp-20-11201-2020 (2020).

Tsigaridis, K. *et al.* The AeroCom evaluation and intercomparison of organic aerosol in global models. *Atmospheric Chemistry and Physics* **14**, 10845-10895, doi:10.5194/acp-14-10845-2014 (2014).

Vakkari, V. *et al.* Major secondary aerosol formation in southern African open biomass burning plumes. *Nature Geoscience* **11**, 580-583, doi:10.1038/s41561-018-0170-0 (2018).

van der Werf, G. R. *et al.* Global fire emissions and the contribution of deforestation, savanna, forest, agricultural, and peat fires (1997–2009). *Atmos. Chem. Phys.* **10**, 11707-11735, doi:10.5194/acp-10-11707-2010 (2010).

Wagstrom, K. M. & Pandis, S. N. Determination of the age distribution of primary and secondary aerosol species using a chemical transport model. *J. Geophys. Res.* **114**, doi:10.1029/2009jd011784 (2009).

Wang, H. *et al.* Aerosols in the E3SM Version 1: New Developments and Their Impacts on Radiative Forcing. *J. Adv. Mod. Earth Syst.* **12**, doi:10.1029/2019ms001851 (2020).

Waquet, F. *et al.* Global analysis of aerosol properties above clouds. *Geophys. Res. Lett.* **40**, 5809-5814, doi:10.1002/2013gl057482 (2013).

Wu, H. *et al.* Vertical variability of the properties of highly aged biomass burning aerosol transported over the southeast Atlantic during CLARIFY- 2017. *Atmos. Chem. Phys.*, doi:10.5194/acp-2020-197 (2020)

Zhang, Y. *et al.* A comparative review of inorganic aerosol thermodynamic equilibrium modules: similarities, di!erences, and their likely causes. *Atmospheric Environment* **34**, 117-137 (1999).

Zheng, G., *et al.,* Long-range transported North American wildfire aerosols observed in marine boundary layer of eastern North Atlantic, *Env. Inter.* **139**, (2020), doi:10.1016/j.envint.2020.105680.

Zhou, S. *et al.* Regional influence of wildfires on aerosol chemistry in the western US and insights into atmospheric aging of biomass burning organic aerosol. *Atmos. Chem. Phys.* **17**, 2477-2493, doi:10.5194/acp-17-2477-2017 (2017).

Zuidema, P. *et al.* Smoke and Clouds above the Southeast Atlantic: Upcoming Field Campaigns Probe Absorbing Aerosol's Impact on Climate. *Bull. Am. Meteor. Soc.* **97**, 1131-1135, doi:10.1175/bams-d-15-00082.1 (2016).

Zuidema, P. *et al.* The Ascension Island Boundary Layer in the Remote Southeast Atlantic is Often Smoky. *Geophys. Res. Lett.* **45**, 4456-4465, doi:10.1002/2017gl076926 (2018).

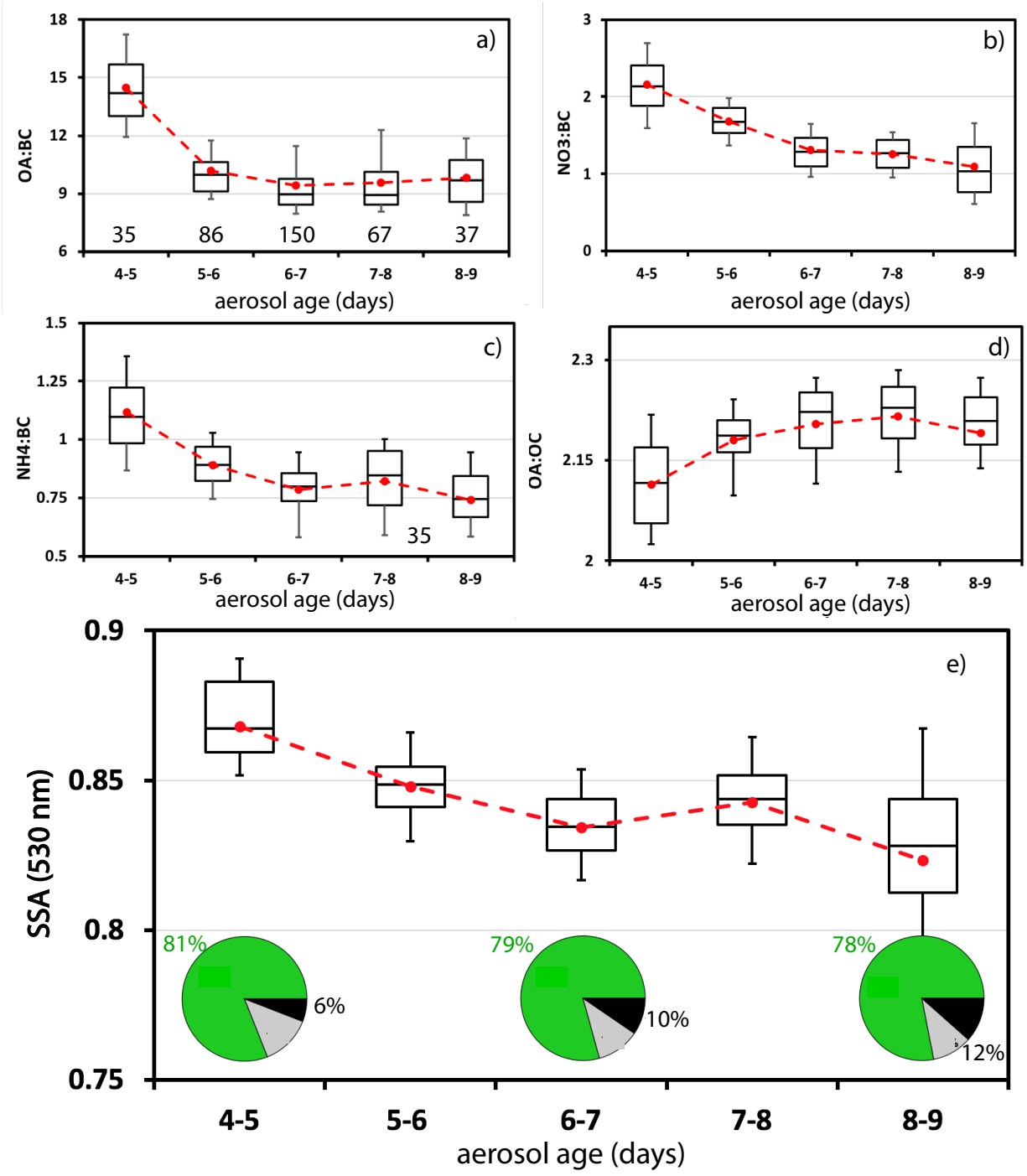

Fig. 1: As aerosol ages, organic aerosol decreases relative to black carbon and the single-scattering-albedo (SSA) decreases. a) OA:BC, b) NO_3:BC, c) NH_4:BC, d) OA:OC, e) top single-scattering albedo (SSA) at 530 nm wavelength, all with respect to model-derived mean age for the selected flights, for OA>20 ug m^{-3} at STP. Data sample size in minutes shown in panel a). Box-whisker plots depict 10, 25, 50, 75, and 90 percentiles, with mean values as red filled circles. Corresponding bulk mass fractional composition (bottom) of OA (green), NO_3 + SO_4 + NH_4 (grey) and BC (black). As aerosol ages, SSA decreases and the relative contribution from black carbon increases.

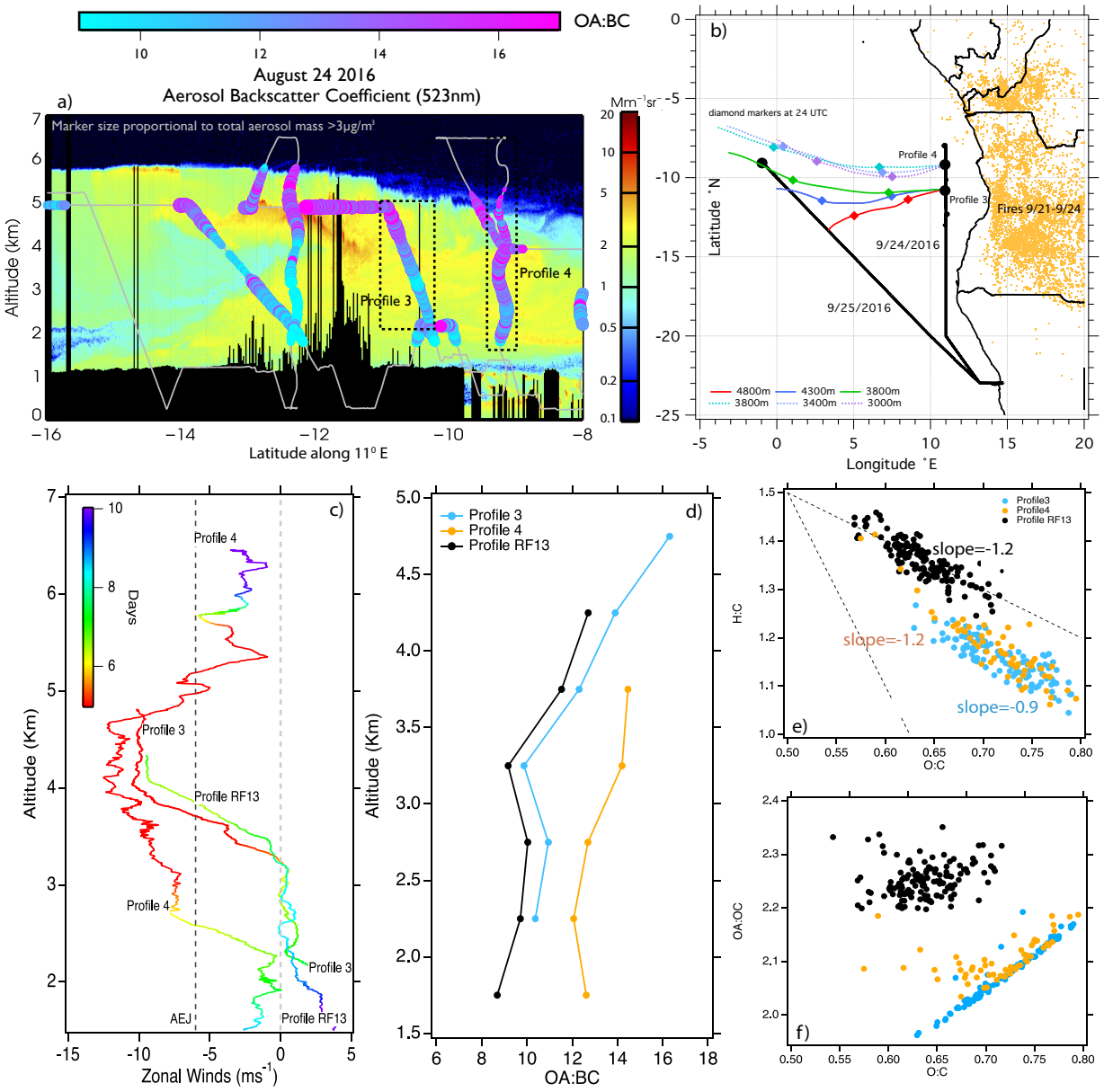

Fig. 2: As aerosol ages during its westward advection by strong free-tropospheric winds, the OA:BC ratio reduces. a) 9/24/2016 flight track superimposed on High Spectral Resolution Lidar-2 aerosol backscatter imagery collected at 11^0E, 10^0 S on an overflying ER-2 plane. b) HYSPLIT forward trajectories beginning 10am (noon) UTC at profile 3 (4) (black solid circles). c) *in-situ* zonal wind profiles from profiles 3, 4, and endpoint of 9/25/2016 track (profile RF13). d) same as c) but for OA:BC (OA>20 ug m^{-3} only). e) van Krevelen diagram of H:C versus O:C for the three profiles indicate oxygenated OA (Lambe et al., 2012); 1:1 dotted line indicates carboxylic acid formation, 2:1 dotted line indicates ketone/aldehyde formation. A slight increase in H:C and decrease in O:C between the two days is accompanied by f) a small increase in OA:OC as O:C decreases. e) and f) both shown using native 5-second resolution data.

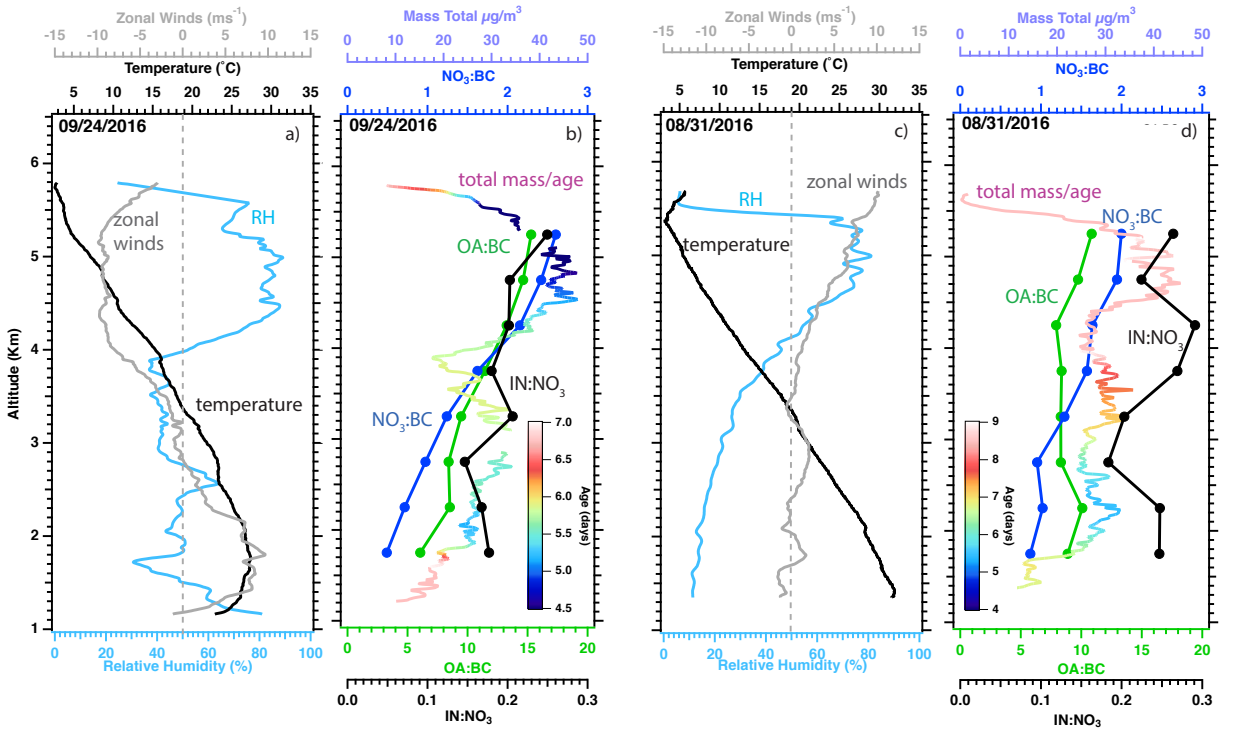

Fig. 3: 24 September, 2016 (12.34^0 S, 11^0 E) vertical profiles of a) relative humidity (%; blue), zonal winds (m s^{-1}; grey) and temperature (˚C), and b) the inorganic nitrate to black carbon ratio (IN:BC; black), organic aerosol to black carbon ratio (OA:BC; green), total nitrate to black carbon ratio (NO_3:BC; blue) averaged every 500 m (approximately 2 minutes of data), and total mass concentration (OA + BC + SO_4 + NO_3 + NH_4 µg/m^3; 1Hz resolution) colored by aerosol age c)-d): same as a)-b) but for 31 August, 2016 (16.4^0 S, 6.5^0 E). Note the different color scales for aerosol age.

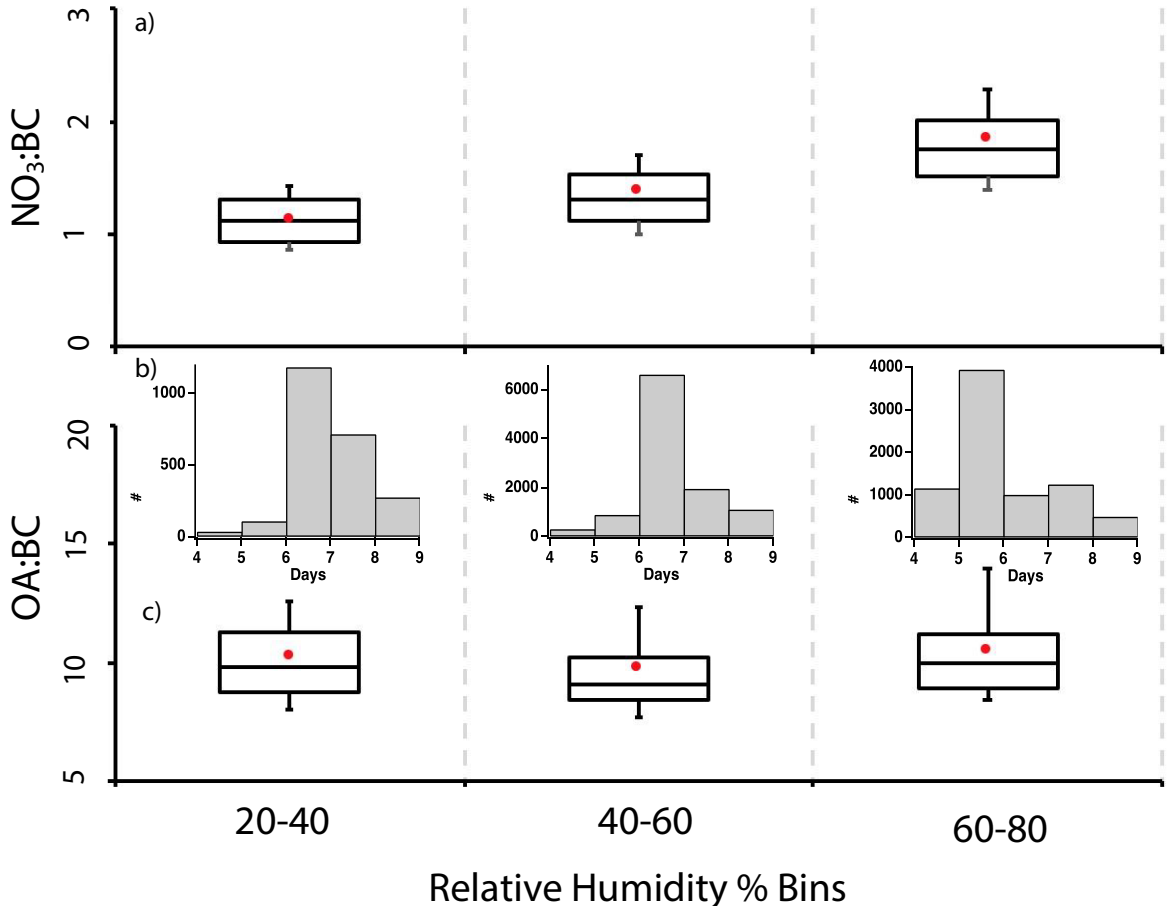

Fig. 4: The lower NO3:BC ratios at lower free-tropospheric relative humidities, occurring at lower, warmer altitudes, could indicate a thermodynamical partitioning to the gas phase, rather than an irreversible loss through photolysis/oxidation. OA:BC does not depend on relative humidity, however, suggesting aging through photolyis/oxidation is dominant. a) NO_3:BC and c) OA:BC ratios for the 6 selected flights as a function of relative humidity, for OA>20 ug m^{-3} at STP. The 10^{th} , 25^{th} , median, 75^{th} and 90^{th} percentiles are indicated using box-whiskers, the mean with solid red circle and marker. b) corresponding distribution of aerosol ages within each relative humidity range.

Methods: Flight Selection and Data Characteristics

Flight and Data Selection

The ORACLES campaign involved 28 total research flights (RF) aboard the NASA P-3B in 2016-2017, with 15 flights during September, 2016 operating out of Walvis Bay, Namibia and 13 flights during August, 2017, operating out of Sao Tome. Approximately one-half of the flights were devoted to a routine pattern, following along an offshore diagonal (20˚S, 10˚E to 10˚S, 0˚E) in September, 2016 (Redemann et al., 2021). Flight selection focused on September conditions, when the African Easterly Jet-South (AEJ-S) is active, with a restricted time frame increasing the likelihood that fire emission source regions are similar. Each selected flight needed to include 20 minutes of free-tropospheric OA>20 ug m^{-3} data, with accompanying fully-functioning SP2 and CO instruments, and HYSPLIT backtrajectories to the originating fire emissions confirming similar source regions. The free troposphere is defined by applying a height threshold for each flight (ranging from 1200 to 1800) and data are further restricted to relative humidities < 80% to exclude aqueous-phase oxidation. This selection criteria led to 6 flights, 5 from 2016 (August 31, September 4, 6, 24 and 25) and August 31, 2017. Flight tracks are shown in Fig. S1. Individual flight tracks indicating the location and estimated age of the selected data, along with meteorological notes drawn from Ryoo et al., (2021), and the aerosol forecast maps used in the field, are shown in Fig. S2.

Other measures of aerosol chemistry highlight the similarities between the flights more strongly. The modified combustion efficiency factors (see Supplementary p. 10-11 for their description) are all above 0.97 for each flight (Fig. S3). The BC:CO ratios are within 30%, decreasing slightly but without statistical insignificance over time (Fig. S5), perhaps because more combustable material is burnt earlier (Eck et al., 2013). The O:C ratio, closely related to the

average carbon oxidation state (Kroll et al., 2011), is statistically similar for the 31 August-25 September, 2016 flights (0.61-0.69, with standard deviations of 0.03-0.06), with only the 31 August, 2017 flight reporting more highly oxidized aerosol, with a mean O:C ratio of 0.81(Fig. S7). Most flights indicate slightly more oxidized aerosol at older aerosol ages. Increasing oxidation with age is also evident in the *f44* value (Fig. S6).

All 6 flights include aerosol with model-estimated age since emission of 6-7 and 7-8 days, supporting an examination of inter-flight variability for reasons other than aging. Flight-mean values of OA:BC aged 7-8 days ranges from a minimum of 7.0 +/- 1.0 on 9/4/2016, to 13.2 +/- 2.4 on 9/25/2016 (Fig. S8). For OA:BC aged 6-7 days, the range is 7.3 +/- 1.0 on 9/4/2016 to 13.8 +/- 1.4 on 9/6/2016 (Fig. S8). These clearly indicate different compositional fractions can occur on individual flights. The individual OA:BC, NO3:BC, NH4:BC and OA:OC ratios, color-coded for each flight day (Fig. S9) further indicate the intra-flight variability of the aerosol composition. In particular, the organic aerosol sampled on 9/25/2016 is more enriched in OA, NO_3 and NH_4 relative to BC than are the aerosols sampled on other flights within the same aerosol age range. Data from this day explains the slight rise in values for an age of 7-8 days in Fig. 1. Nevertheless, in only the 9/24/2016 and 9/25/2016 flights, the OA:BC ratio is clearly lower for aerosol aged 7-8 days compared to 6-7 days, and in all flights except 9/25/2016, the OA:BC is less after the aerosol is aged at least 6 days, compared to that at 4 days.

Weather Research and Forecasting Aerosol Aware Microphysics (WRF-AAM) Model.

Model-derived estimates for aerosol time since emission (age) of up to two weeks were calculated using the campaign's operational aerosol forecast model, the Weather Research and Aerosol Aware Microphysics (WRF-AAM) Model (Thompson and Eidhammer, 2014). The

model releases tracers tagged to CO at the location of emission for each day of a two-week forecast. The model configuration is similar to that in Saide et al, (2016), with the 12-km spatial resolution regional model encompassing a domain (41^0S-14^0N, 34^0W-51^0E) sufficiently large to capture almost all contributing fires. The model is driven by the National Center for Environmental Prediction Global Forecasting System meteorology and daily smoke emissions from the Quick Fire Emissions Dataset (Darmenov and da Silva, 2013) released into the model surface layer. These are advected thereafter according to the model physics, with their spatial distribution constrained near real-time with satellite-derived optical depths. This allows a diurnal cycle representation of the daytime burning. The capabilities of WRF-AAM include photochemistry, particulate matter, optical properties, radiative forcing, aerosol radiation and cloud chemistry feedback, and aerosol-cloud interactions (Grell et al., 2005; Wang et al., 2015).

Sampling Inlet

A high-resolution aerosol mass spectrometer, nephelometers, absorption and soot photometers, and CO/CO2 analyzer were all situated behind a Solid Diffuser Inlet (SDI), with the nephelometers located closest to the inlet and the AMS and SP2 located ~8m behind the inlet. The SDI brings ambient aerosol into the aircraft and can efficiently transmit aerosol particles smaller than 4μm in dry diameter (McNaughton et al., 2007). The SDI and ground-sampled submicron scattering data agreed to within 16% during the DC-8 Inlet Characterization Experiment (McNaughton et al., 2007). This establishes the particle loss to the inlet structure, instrument and tubing layout during the ORACLES campaign. Additionally, the sample flow through the inlet was measured and adjusted to ensure the air velocity equaled the flight speed to within 5%. This isokinetic sampling minimizes size-dependent sampling biases (Huebert et al.,

70 1990). Although the inlet was maintained at isokinetic flow, the instruments required a constant
71 flow. An online particle loss calculator (Aerocalc, created by Paul Baron,
72 http://www.tsi.com/uploadedFiles/Product_Information/Literature/Software/Aerocalc2001.xls)
73 selected tubing material, length, and diameter to minimize particle loss between the SDI and
74 aircraft instruments. The inlet was anodized aluminum, with the flow split into tubes of stainless
75 steel. All lines to the mass spectrometer relied on ½" stainless steel (outer diameter) and ¼"
76 (outer diameter) copper tubing, to reduce the possible presence of extraneous organic
77 compounds. The conductive tubing also minimizes electrophoretic losses. Tubing to the
78 scattering, sizing and counting instruments consisted of graphite-impregnated silicone tubing,
79 with condensation of any released organic compounds upon particles within the air stream
80 unlikely to affect the particle size over the short distance. Due to differences in flow rates and
81 paths, additional losses may affect some instruments more than others. Figures S12-S13 show
82 the plumbing diagram of the aerosol instruments for each year. Calculated losses were
83 negligible, if inherently optimistic and unable to account for all features of the hardware and
84 instruments.

85 For the AMS, its ~8 m distance from the SDI increased the potential for particle wall
86 losses (Fig. S12 and S13). The mass scattering efficiency from wall losses is accounted for using
87 the ratio of the submicron scattering at 500 nm (Mm^{-1}) from two TSI nephelometers (model
88 3563) to the total of the AMS and SP2-derived aerosol and black carbon mass concentrations.
89 The submicron aerosol is assumed to scatter ~5 Mm^{-1} at a wavelength of 500 nm per $\mu g/m^3$ of
90 aerosol (Reid et al., 1998; Haywood et al., 2003a). The nephelometers were close to the aerosol
91 inlet, where particle loss is assumed to be minimal. The nephelometer closest to the aerosol inlet
92 measured total scattering, while a second nephelometer in series with the first measured both

total and submicron scattering. The second nephelometer measured a ratio of total to submicron scattering of 1.02 in the free troposphere, indicating little contribution from coarse aerosol. The submicron mass scattering efficiency by the nephelometer closest to the aerosol inlet was estimated using this ratio at three different locations/altitudes per flight. The average mass scattering efficiency of 5.92 is close to the expected value of 5, and constrains wall losses to within 20% for the entire campaign.

Aerosol Mass Spectrometer

The Hawaii Group for Environmental Aerosol Research (HiGEAR) operated an Aerodyne High-Resolution Time-of-Flight Aerosol Mass Spectrometer (HR-ToF-AMS, hereafter referred to as AMS) during ORACLES, building on previous experience in the southeast Pacific (Yang et al., 2011; Shank et al., 2012) and the Arctic (Howell et al., 2014). The AMS sampled the chemical composition of non-refractory aerosols with vacuum aerodynamic diameters between approximately 70 nm to 700 nm at a rate of ~1.38 $cm^3 s^{-1}$. An aerodynamic lens selects and focuses particles at a constant 600 hPa pressure onto a 650°C heated surface. The non-refractory particles are then evaporated off the heated surface and ionized through electron impaction at 70 eV; the ions are carried forward and analyzed further, with some particles, such as soot, some organics, dust, and some salts remaining unvaporized (and unanalyzed). A 'V-mode' operation provided a higher time resolution for the same signal-to-noise, with only a modest loss in the mass resolution (see DeCarlo et al., 2006 for more description). The AMS chopper alternately open and closed every two seconds, to allow aerosol into the AMS and to then analyze it, with an additional second separating each duty cycle. This produces a native time resolution of approximately five seconds, with the data thereafter interpolated onto a one-second temporal grid to facilitate integration with other datasets.

116 The bulk mass (not size-resolved) chemical species measurements are primarily processed using
117 a specifically-designed data analysis software known as SeQUential Igor data RetRiEval
118 (SQUIRREL, v.1.57l; Allan et al., 2003, 2004), with the Peak Integration by Key Analysis
119 (PIKA) program (v.1.16; DeCarlo et al., 2006) resolving the O:C, H:C and OA:OC ratios. The
120 analysis relies on analysis package Igor Pro (version 6.37).
121 Further considerations for the ORACLES AMS-derived aerosol mass concentration data
122 accuracies include the instrument detection threshold, calibrations, and discrimination for
123 organic versus inorganic nitrate. These are considered in that order. Many of the data quality
124 assurance procedures follow those within Shank et al., (2012).
125 The aircraft-based background values are determined from the noise levels measured at
126 15,000 ft during a 10-minute time period on the 4 September, 2016 flight. This established
127 detection limits of 0.15μg/m^3 for organics, 0.04μg/m^3 for nitrate, 0.03μg/m^3 for sulfate, and
128 0.01μg/m^3 for ammonium. Detection limits typically improve during a flight as the background
129 material becomes effused. The AMS was heated pre-flight during the 2016 campaign to
130 eliminate material built up in between flights. During the 2017 campaign, an initial high-altitude
131 remote sensing leg provided time to drive off extraneous material before beginning the *in-situ*
132 sampling.
133 The AMS was calibrated twice during the 2016 campaign (at the beginning and end), and
134 after every 2-3 flights during the 2017 campaign for a total 8 calibrations, using ammonium
135 nitrate particles. An ammonium nitrate solution is sent through an atomizer to produce desiccated
136 submicron aerosol that is then sent to the AMS. A long differential mobility analyzer (LDMA)
137 (TSI 3934) selects for 300 nm diameter particles, and a condensation nuclei counter (TSI3010)
138 measures the aerosol number concentration. The ammonium nitrate aerosol is diluted by a factor

of four in the atomizer to create a calibration curve. The ionization efficiency (IE) of nitrate is thereafter calculated from the aerosol mass and number concentrations. The ionization efficiency estimates the number of ions from a known amount of mass entering the AMS using the ion signals at *m/z* peak 30 (NO^+) and 46 (NO_2^+). The nitrate IE values centered on $1.31e^{-7}$, with a nominal 10% uncertainty assigned to it following Bahreini et al., (2009), and slightly higher than the $1e^{-7}$ value within Alfarra et al., (2004). The ionization efficiencies for ammonium, sulfate and organics relative to those for nitrate are thereafter determined within SQUIRREL as: 4 for NH_4; 1.1 for measured nitrate relative to the calibration value; 1.2 for SO_4; and 1.4 for organics, following Jimenez (2010).

A time- and composition-dependent collection efficiency (CE) corrects for the incomplete vaporization of mixed phase particles (Middlebrook et al., 2012), as liquid aerosol is less likely to bounce off the heater and more likely to escape detection than is neutralized aerosol (Huffman et al., 2005, Drewnick et al. 2003). Liquid aerosol is primarily acidic, and the acidity of the free-tropospheric aerosol is assessed by comparing the molar ratio of NH_4 to NO_3+2xSO_4 (Fig. S14). This is a simplification of the $NH_{4,measured}/NH_{4,predicted}$ relationship put forth in Zhang et al., (2017), with the contribution of chloride neglected because it is small. $NH_{4,predicted}$ is the amount of ammonium required to neutralize the inorganic anions observed by the AMS. The applied collection efficiency, $CE=max(0.5, 1- NH_4/(2xSO_4)$, also neglects the small nitrate contribution, and establishes 0.5 as the lower limit, consistent with most field campaigns (Middlebrook et al., 2012). The ratio of the measured ammonium to the molar sum of nitrate and 2*sulphate is mostly below 1, but rarely below 0.75 (Fig. S14), typically establishing a CE of 0.5. The mildly acidic aerosol suggests mild suppression of inorganic acid formation. Wu et al., (2020) report nitrate aerosol that is fully neutralized based on independent AMS measurements

from August-September 2017 further west of the ORACLES sampling, above Ascension Island (8^0S, 14.5^0W). This indicates further loss of the organic nitrate may be occurring between the ORACLES and Ascension locations. The CE values for the other species are set to 0.5; Middlebrook et al., (2012) do not find any dependence of the CE on the mass fraction of organics.

The overall uncertainty to the reported aerosol mass concentrations is hereafter estimated at 33% to 37%, at a one-minute time resolution, based on Bahreini et al., (2009). This is likely dominated by the uncertainty in CE, with additional uncertainty in the organic RIE. Each age range contains over 30 minutes of data (Fig. 1), for a standard error of the mean of less than 7%, corresponding to an uncertainty in OA:BC of approximately 0.07, significantly less than the OA:BC loss observed per day between days 4-7 (Fig. 1), and further supporting that most of the range in the OA:BC values comes from inherent differences in initial OA production between individual flights (Fig. S3).

Farmer et al., (2010) provide an approach for estimating the contribution to the total nitrate signal from organic nitrate (ON) using the NO^+:NO_2^+ ratio, building on the observation that organic nitrates typically fragment into larger proportions of NO^+ than do inorganic nitrates (in their study, organic NO^+ ratios vary between 1.8 to 4.6 for different organonitrates, compared to 1.5 for NH_4NO_3). Their Equation 1, reproduced below, provides an estimate of the ON fraction that can be readily applied to the ORACLES AMS data, assuming that the ON fraction can be resolved. The success of this approach also assumes that those inorganic nitrates also capable of providing a large NO^+ ratio, such as mineral nitrates, are not present. Both assumptions are justified for the SEA free troposphere.

$$\text{X (ON \%)} = \frac{(R_{obs} - R_{NH_4NO_3})(1+R_{ON})}{(R_{ON} - R_{NH_4NO_3})(1+R_{obs})} \quad (1)$$

185 R_{obs} is the ORACLES *m/z* ratio of ion fragments 30 to 46, R_{NH4NO3} is the IE calibration-derived
186 ratio (1.26 for 2016 and 1.545 for 2017) and an R_{ON} value of 3.41 is a reference ratio based on
187 the average fragmentation pattern into the NO^+:NO_2^+ ratios for the OIA-HN, OIA-CN and OIA-
188 olig standards evaluated within Table S1 of Farmer et al. (2010). The IN fraction is 1-ON.

189 **Single Particle Soot Photometer**

190 Mass concentrations of refractory black carbon[4] (rBC) particles with volume equivalent
191 diameters between ~80 and 500 nm, assuming a rBC density of 1.8 g cm^{-3}, were measured via
192 laser-induced incandescence and calibrated with fullerene soot (Alfa Aesar; stock: #40971. lot#:
193 F12S011). The SP2 was calibrated using fullerene soot effective density estimates from Gysel et
194 al. (2011). A 4-channel single particle soot photometer (SP2, Droplet Measurement Technology;
195 Schwartz et al., 2006) was deployed by HiGEAR for the 2016 campaign, and an 8-channel SP2,
196 which allows further resolution of the black carbon coatings, was deployed for the 2017
197 campaign.

198 **Optical Instruments: Nephelometers and Particle Soot Absorption Photometers**

199 The absorption angstrom exponent used the spectral light absorption coefficient of the
200 total aerosol at three wavelengths (470, 530, and 660nm) from Particle Soot Absorption
201 Photometers (PSAP; Radiance Research) Wavelength-averaged (as opposed to wavelength-
202 specific) PSAP absorption corrections follow Virkkula, (2010), as per Pistone et al., 2019. The
203 wavelength averaged AAE used Absorption (σ_a) at the 470, 530 and 660nm wavelengths (λ) to
204 calculate a linear fit to $\log(\sigma_a)$ versus $\log(\lambda)$. The 2016 campaign deployed two PSAPs, with
205 their average measurements used, while for 2017 calculations, only the functioning PSAP was
206 used.

The single-scattering albedo, calculated at 530 nm wavelength, relied on TSI nephelometer measurements at (470, 550, 700) nm wavelengths, interpolated to 530 nm using a linear regression in log-log space. Two TSI nephelometers (model 3563, owned by HiGEAR) were deployed; data from the one measuring scattering from all sized particles continuously was used for the SSA calculation. Measurements were corrected according to Anderson and Ogren (1998). All measurements reflect a low (~50%) relative humidity.

CO/CO_2 Analyzer

Carbon monoxide is measured with an aircraft modified gas-phase $CO/CO_2/H_2O$ Analyzer (ABB/Los Gatos Research $CO/CO_2/H_2O$ Analyzer (907-0029)), operated and analyzed by NASA Ames (Jim Podolske). The analyzer uses a patented Integrated Cavity Output Spectroscopy (ICOS) technology to make stable cavity-enhanced absorption measurements of CO, CO_2, and H_2O in the infrared spectral region. The instrument reports CO mixing ratio (mole fraction) at a 1-Hz rate based on measured absorption, gas temperature, and pressure using Beer's Law (Zellweger et al., 2012). The measurement precision is 0.5 ppbv over 10 seconds.

CO and CO_2 are used to calculate the modified combustion efficiency (MCE), a measure of fire emission conditions (Collier et al., 2016; Yokelson et al., 1997).

$$MCE = \Delta CO_2 / (\Delta CO + \Delta CO_2) \quad (2)$$

where ΔCO and ΔCO_2 represent the measured CO and CO_2 amounts, in moles, relative to background values. Higher values of MCE (>0.9) are associated with flaming combustion, whereas values less than 0.9 are more typical of smoldering combustion, for which more particles are typically emitted for the same amount of fuel. Adopted background values were 65 (77) ppbv for CO, and 397 (404) ppmv for CO_2, in 2016 (2017), based on measurements in the

free troposphere above any smoke plumes (~7000m). Equation 2 can be rewritten as Eq. 3, with a regression used to estimate the $\Delta CO / \Delta CO_2$ value.

$$MCE = 1 / (1 + \Delta CO / \Delta CO_2) \quad (3)$$

References: **Methods**

Alfarra, M. R. *et al.* Characterization of urban and rural organic particulate in the Lower Fraser Valley using two Aerodyne Aerosol Mass Spectrometers. *Atmos. Env.,* **38**, 5745-5758, doi:10.1016/j.atmosenv.2004.01.054 (2004).

Anderson, T. L. & Ogren, J. A. Determining Aerosol Radiative Properties Using the TSI 3563 Integrating Nephelometer. *Aer. Sci. Tech.,* **29**, 57-69, doi:10.1080/02786829808965551 (1998).

Bahreini, R. *et al.* Organic aerosol formation in urban and industrial plumes near Houston and Dallas, Texas. *J. Geophys. Res.,* **114**, doi:10.1029/2008jd011493 (2009).

Collier SZ, T. B. Onasch, D. A. Jaffe, L. Kleinman,, A. J. Sedlacek III NB, J. Hee, E. Fortner, J. E. Shilling, D. Worsnop, Robert J. Yokelson, C. Parworth, X. Ge, Jianzhong Xu,, Z. Butterfield DC, M. K. Dubey, M. Pekour, S. Springston, Qi Zhang. Regional Influence of aerosol emissions from wildfires driven by combustion efficiency: insights from the BBOP campaign. *Env. Sci. Tech.,* 2016, **50**(16)**:** 8613-18622.

DeCarlo, P. F. *et al.* Field-deployable, high-resolution, time-of-flight aerosol mass spectrometer. *Anal Chem* **78**, 8281-8289, doi:10.1021/ac061249n (2006).

Drewnick, F. *et al.* A New Time-of-Flight Aerosol Mass Spectrometer (TOF-AMS)—Instrument Description and First Field Deployment. *Aer. Sci. Tech.,* **39**, 637-658, doi:10.1080/02786820500182040 (2005).

Eidhammer, T. & Thompson, G. A Study of Aerosol Impacts on Clouds and Precipitation Development in a Large Winter Cyclone. *J. Atmos. Sci.,s* **71**, 3636-3658, doi:10.1175/jas-d-13-0305.1 (2014).

Grell GA, Peckham SE, Schmitz R, McKeen SA, Frost G, Skamarock WC*, et al.* Fully coupled "online" chemistry within the WRF model. *Atmos. Env.,* 2005, **39**(37)**:** 6957-6975.

Gysel, M., Laborde, M., Olfert, J. S., Subramanian, R. & Gröhn, A. J. Effective density of Aquadag and fullerene soot black carbon reference materials used for SP2 calibration. *Atmos. Meas. Tech. Disc.,* **4**, 4937-4955, doi:10.5194/amtd-4-4937-2011 (2011).

Howell, S. G. *et al.* An airborne assessment of atmospheric particulate emissions from the processing of Athabasca oil sands. *Atmos. Chem. Phys.,* **14**, 5073-5087, doi:10.5194/acp-14-5073-2014 (2014).

Huebert BJ, Lee G, Warren WL. Airborne Aerosol Inlet Passing Efficiency Measurement. *J. Geophys. Res.,* 1990, **95**(D10)**:** 16369-16381.

Huffman, J. A. *et al.* Design, Modeling, Optimization, and Experimental Tests of a Particle Beam Width Probe for the Aerodyne Aerosol Mass Spectrometer. *Aer.l Sci. Tech.,* **39**, 1143-1163, doi:10.1080/02786820500423782 (2005).

Kroll, J., Donahue, N., Jimenez, J. *et al.* Carbon oxidation state as a metric for describing the chemistry of atmospheric organic aerosol. *Nature Chem* **3,** 133–139. doi:10.1038/nchem.948 (2011).

Middlebrook, A. M., Bahreini, R., Jimenez, J. L. & Canagaratna, M. R. Evaluation of Composition-Dependent Collection Efficiencies for the Aerodyne Aerosol Mass Spectrometer using Field Data. *Aer. Sci. Techn.* **46**, 258-271, doi:10.1080/02786826.2011.620041 (2012).

McNaughton, C. S. *et al.* Results from the DC-8 Inlet Characterization Experiment (DICE): Airborne Versus Surface Sampling of Mineral Dust and Sea Salt Aerosols. *Aer. Sci. Tech.,* **41**, 136-159, doi:10.1080/02786820601118406 (2007).

Reid, J. S. *et al.* Physical, chemical, and optical properties of regional hazes dominated by smoke in Brazil. *J. Geophys. Res.,* **103**, 32059-32080, doi:10.1029/98jd00458 (1998).

Schwarz, J. P. *et al.* Single-particle measurements of midlatitude black carbon and light-scattering aerosols from the boundary layer to the lower stratosphere. *J. Geophys. Res.,* **111**, doi:10.1029/2006jd007076 (2006).

Shank, L. M. *et al.* Organic matter and non-refractory aerosol over the remote Southeast Pacific: oceanic and combustion sources. *Atmos. Chem. Phys.,* **12**, 557-576, doi:10.5194/acp-12-557-2012 (2012).

Silva, A. S. D. A. d. The Quick Fire Emissions Dataset (QFED): Documentation of versions 2.1, 2.2 and 2.4. 1-201 (NASA Goddard Space Flight Center, 2015).

Virkkula, A.: Correction of the Calibration of the 3-wavelength Particle Soot Absorption Photometer (3 PSAP), Aerosol Sci. Tech., 44, 706–712, 2010.

Wang K, Zhang Y, Yahya K, Wu S-Y, Grell G. Implementation and initial application of new chemistry-aerosol options in WRF/Chem for simulating secondary organic aerosols and aerosol indirect effects for regional air quality. *Atmos. Env.,* 2015, **115:** 716-732.

Yang, M. *et al.* Atmospheric sulfur cycling in the southeastern Pacific – longitudinal distribution, vertical profile, and diel variability observed during VOCALS-REx. *Atmos. Chem. Phys.,* **11**, 5079-5097, doi:10.5194/acp-11-5079-2011 (2011).

Yokelson RJ, Susot RA, Ward DE, Reardon JJ, Griffith DWT. Emissions from Smoldering Combustion of Biomass Measured by Open-Path Fourier Transform Infrared Spectroscopy. *J. Geophys. Res.,* 1997, **102**(18)**:** 865-877.

Zellweger C, Steinbacher M, Buchmann B. Evaluation of new laser spectrometer techniques for in-situ carbon monoxide measurements. *Atmos. Meas. Tech.* 2012, **5**(10)**:** 2555-2567.

Zhang, Q., Jose L. Jimenez, Douglas R. Worsnop, and Manjua Canagaranta A Case Study of Urban Particle Acidity and Its Influence on Secondary Organic Aerosol. *Environ Sci Technol* **41**, 3213-3219, doi:10.1021/es061812j (2007).

Supplementary Figures

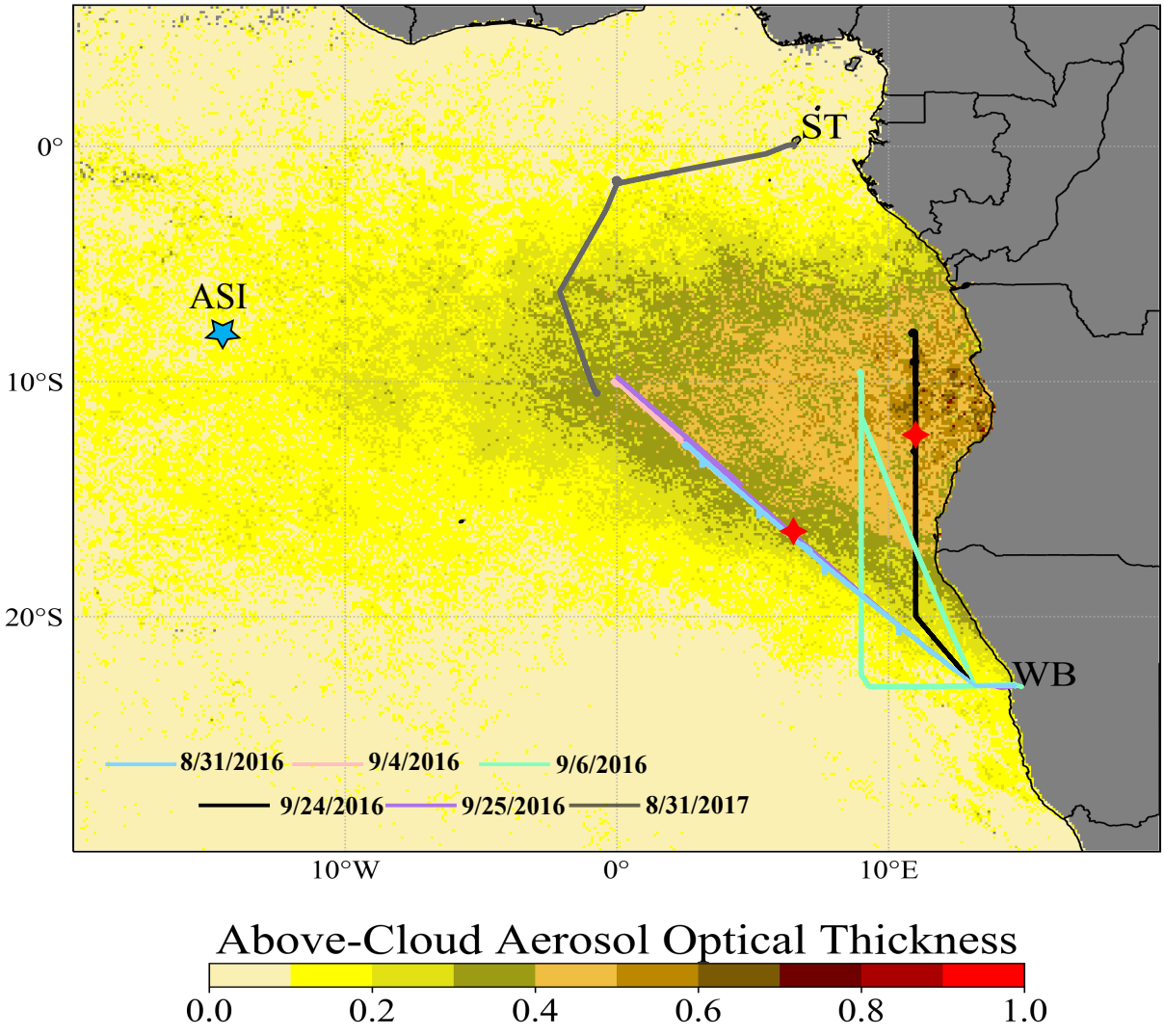

Supplementary Figure S1. Terra MODIS Above Cloud Aerosol Optical Depth (Meyer, 2015) for September 2016 overlaid with selected flight tracks. Locations of the profiles and their corresponding flights selected for Fig. 4 are indicated with red diamonds. ST=Sao Tome; WB=Walvis Bay; ASI=Ascension Island.

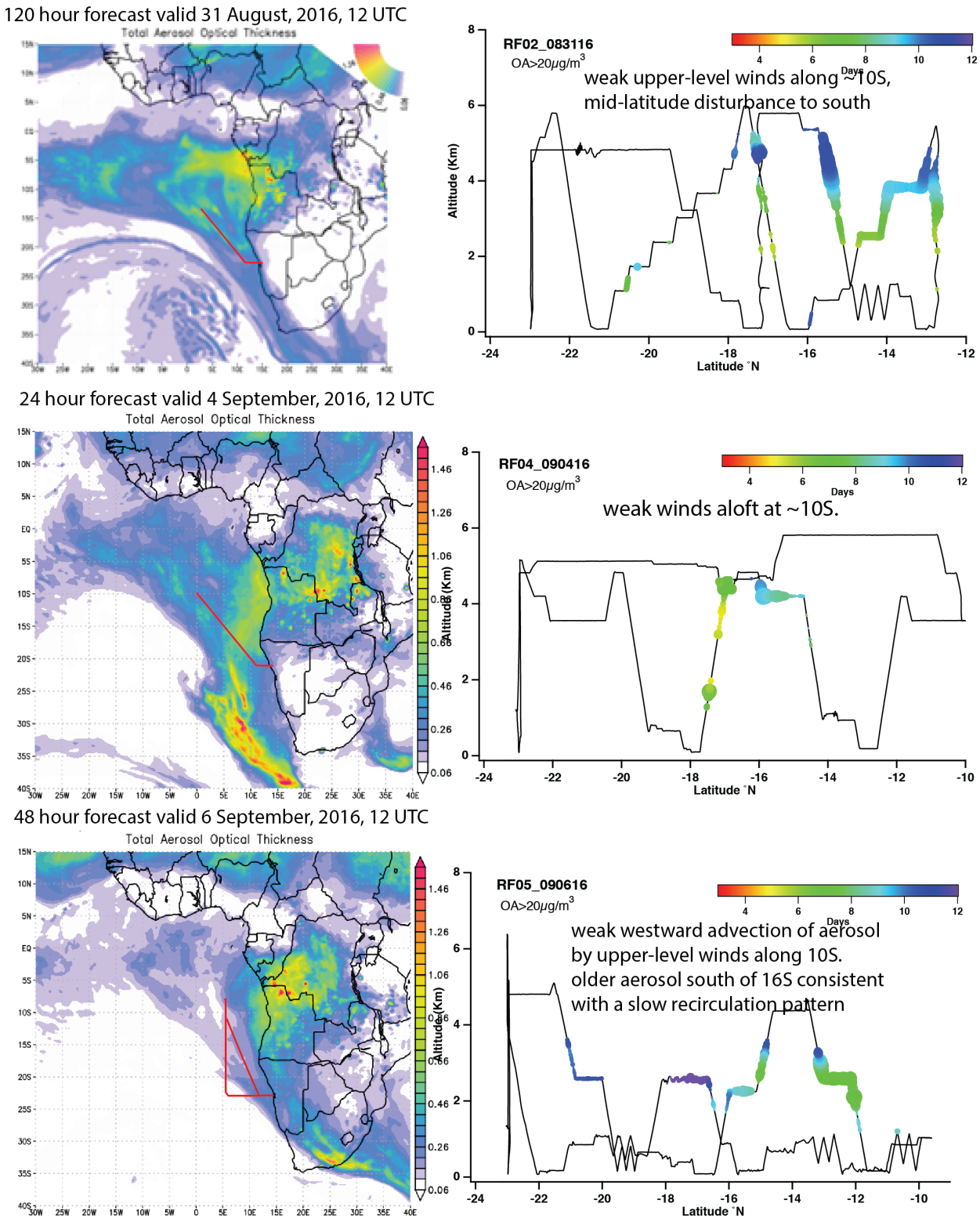

Supplementary Figure S2a: left) GMAO (spell) aerosol optical thickness forecasts for 31 August, 2016; 4 September, 2016; 6 September, 2016. Right) corresponding observed OA colorized to indicate age on the flight altitude versus latitude track.

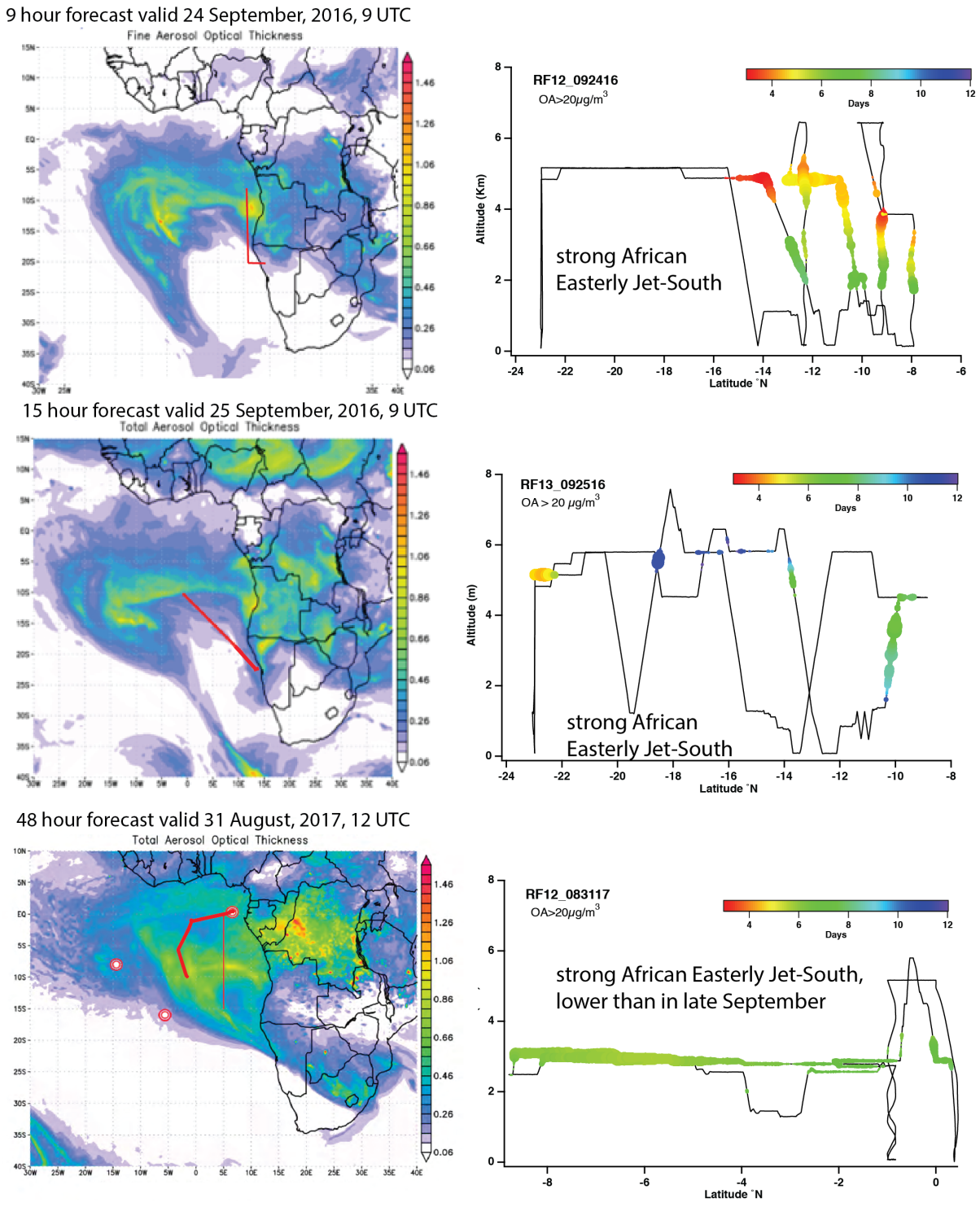

Supplementary Figure S2b: same as Fig S3a but for 24 September, 2016; 25 September, 2016, and 31 August, 2017.

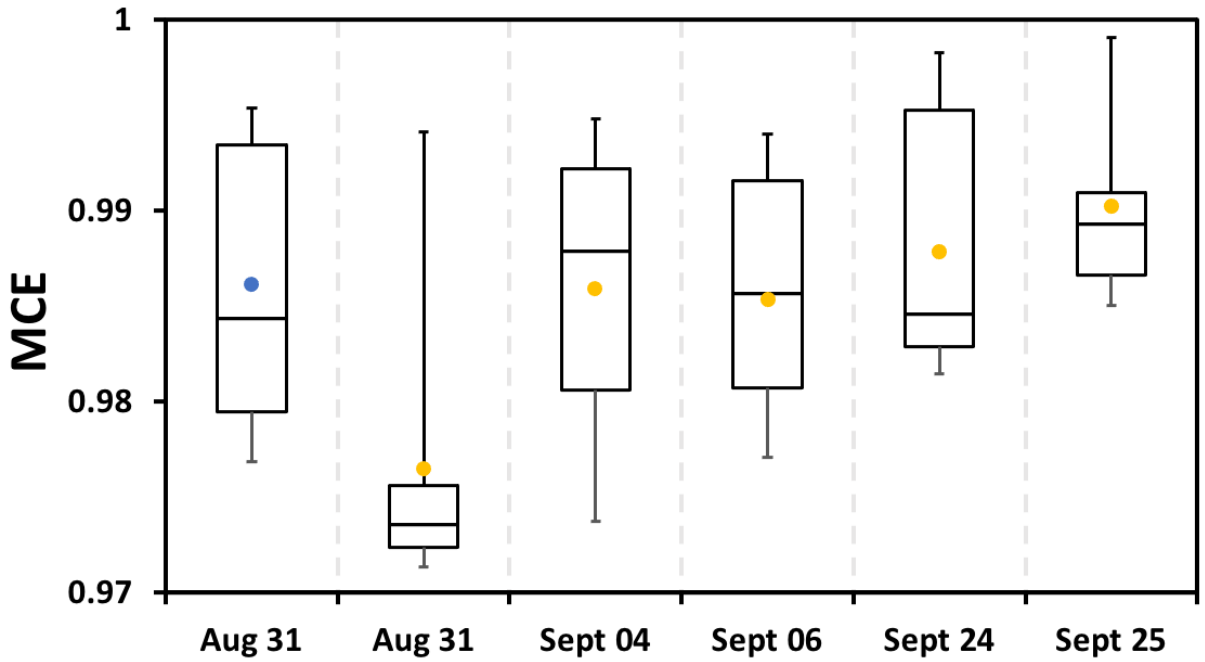

Supplementary Figure S3. Modified combustion efficiency (MCE; see Methods) values for indicated flights. Whiskers represent the 10th and 90th percentiles, boxes illustrate the 75th and 25th percentiles with a line indicating the median and blue (2017) and yellow (2016) filled circles representing the mean. OA>20μg/m^3 only.

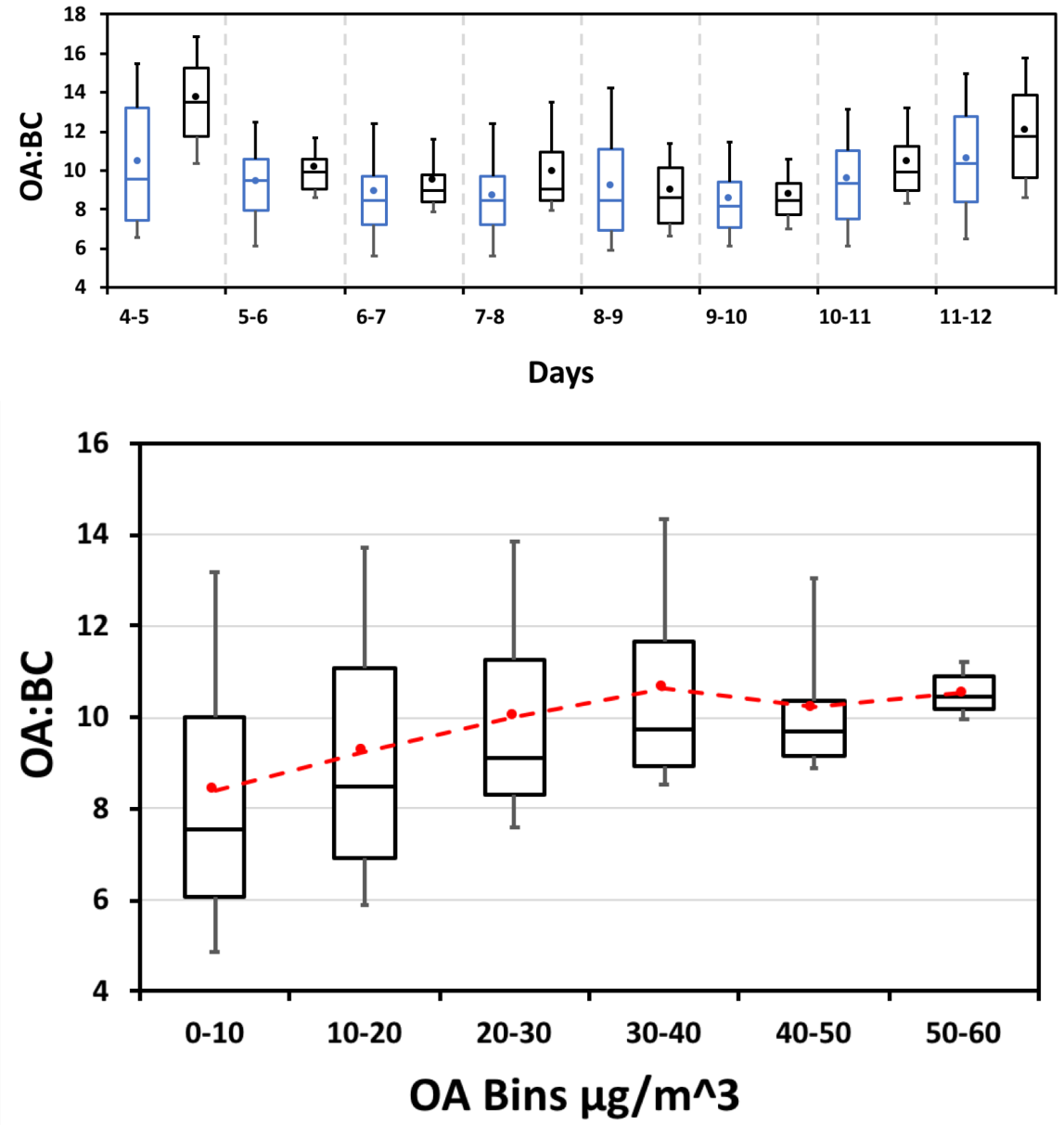

Supplementary Figure S4: a) OA:BC as a function of model age for OA > 3 ug m^{-3} (blue) and OA >20 ug m^{-3} (black). b) OA:BC composited by aerosol mass bins, shown using 10, 25, 50, 75 and 90th percentiles, with means in red.

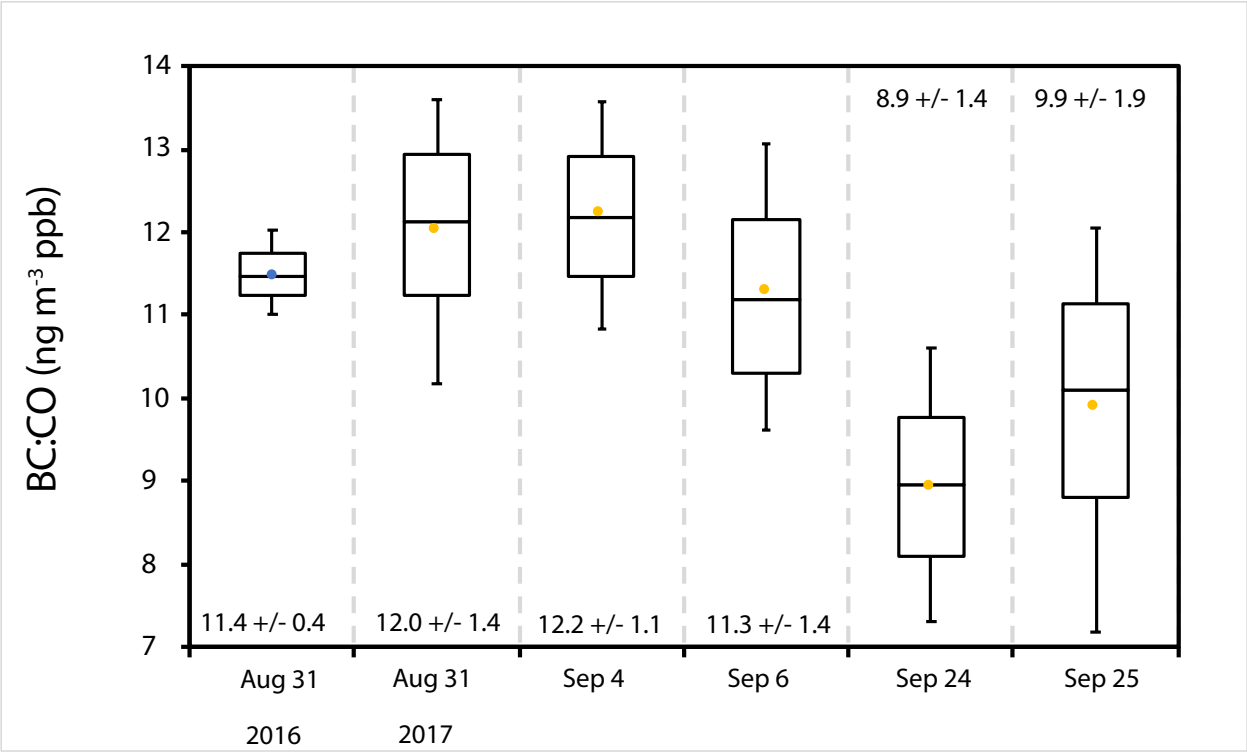

Supplementary Figure S5. BC:CO ratios (units of ng m^{-3} per ppb) for indicated flights. Whiskers represent the 10th and 90th percentiles, boxes illustrate the 75th and 25th percentiles with a line indicating the median and blue (2017) and yellow (2016) filled circles representing the mean. OA>20µg/m^3 only. Mean and standard deviations indicated for each flight.

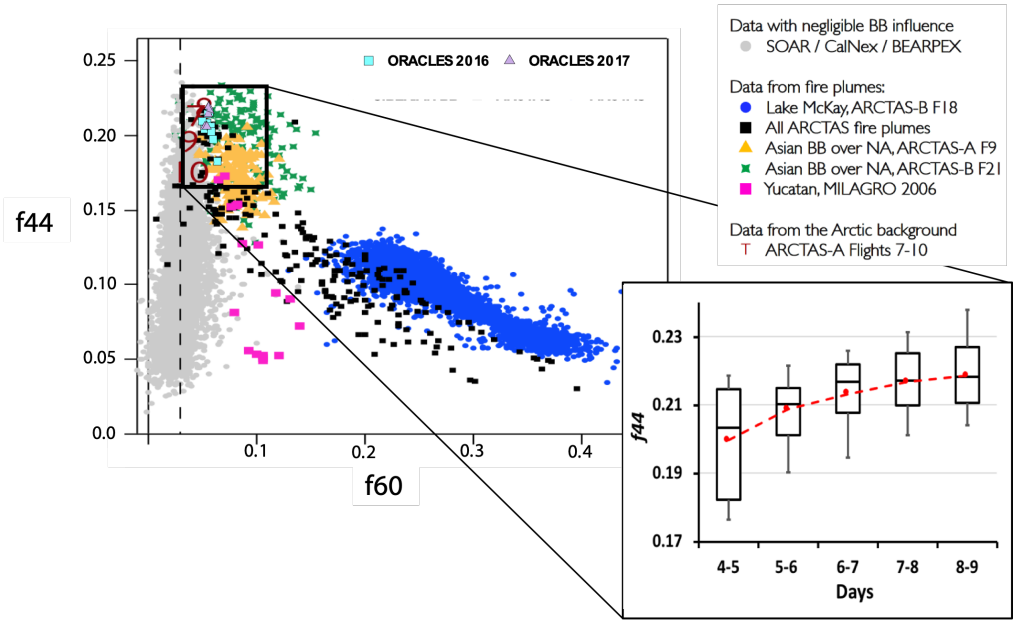

Supplementary Figure S6: top left) *f44* versus *f60* for multiple campaigns, adapted from Fig. 4 of Cubison et al., 2011, overlaid with flight-averaged values from ORACLES (August 2017-grey filled triangles; 2016-light blue filled squares; these include more than just the 6 flights selected for this study). Numbered flights from ARCTAS-A represent 2-week old Siberian biomass burning smoke sampled in northern America, examined in more detail within Cubison et al., 2011. bottom right) ORACLES *f44* values as a function of model-derived age, shown using 10th, 25th, median, 75th and 90th percentiles (box-whisker plots) and mean values (connected red filled circles), from the 6 selected flights, for OA>20 ug m-^{3}. ORACLES *f44* values indicate oxidation processes continue even after four days while *f60* values do not change with model-derived aerosol age (not shown). This is consistent with chamber studies reporting lifetimes of *f44* and *f60* of approximately 20 days and 10 hours, respectively (Hodshire et al., 2019; George and Abbatt, 2010). Although *f44* can serve as a robust physically-based proxy for BBA age, the model-derived particle age provides a clearer time measure, and remains our primary indicator of aerosol age.

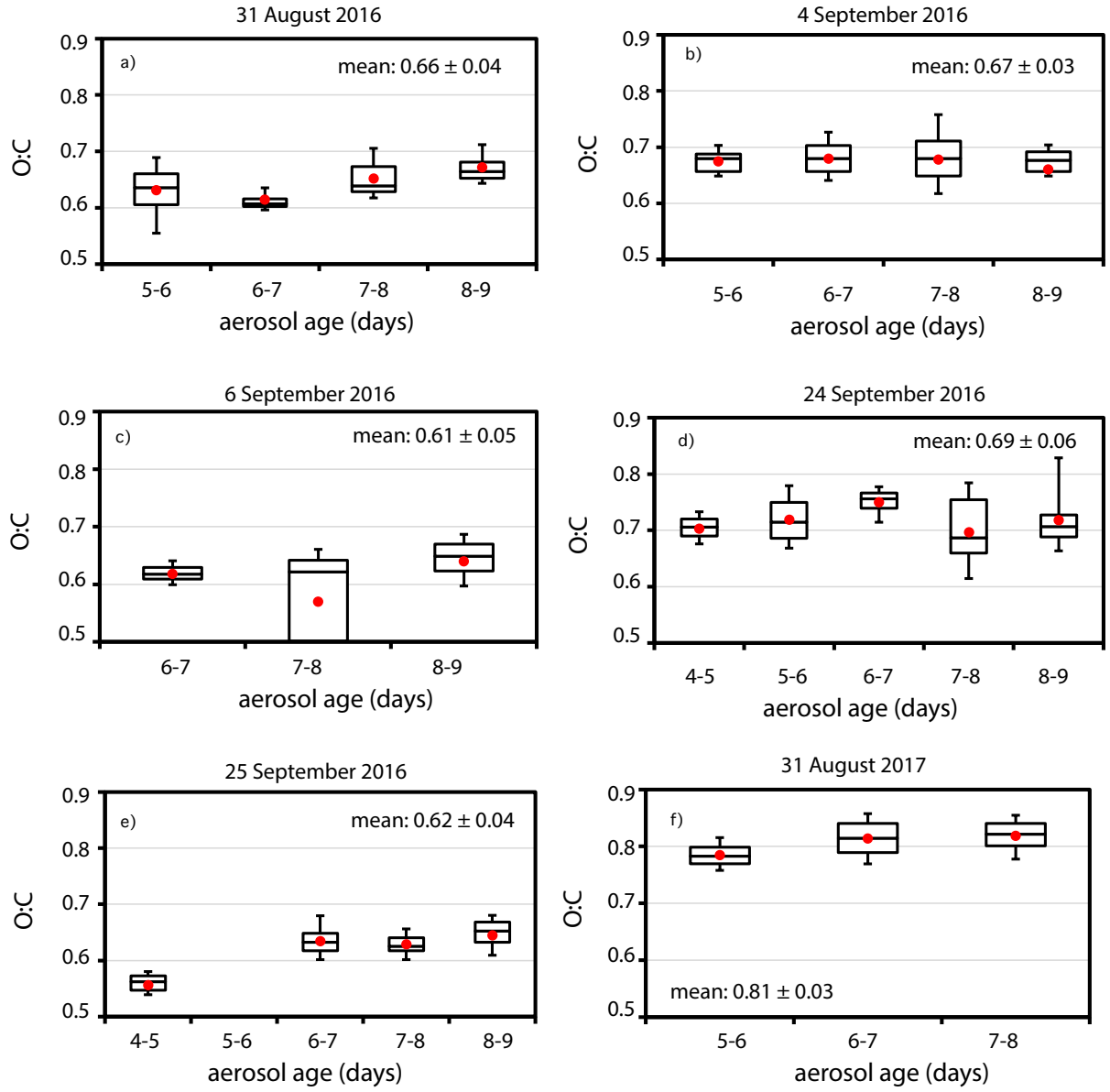

Supplementary Figure S7: O:C versus model-derived age for OA>20µg/m³ for a) 8/31/2016, b) 9/4/2016, c) 9/6/2016, d) 9/24/2016, e) 9/25/2016, and f) 8/31/2017. Whiskers represent the 10th and 90th percentiles, boxes illustrate the 75th and 25th percentiles with a line indicating the median and a red marker the mean. Flight-mean values and their standard deviations included in each panel.

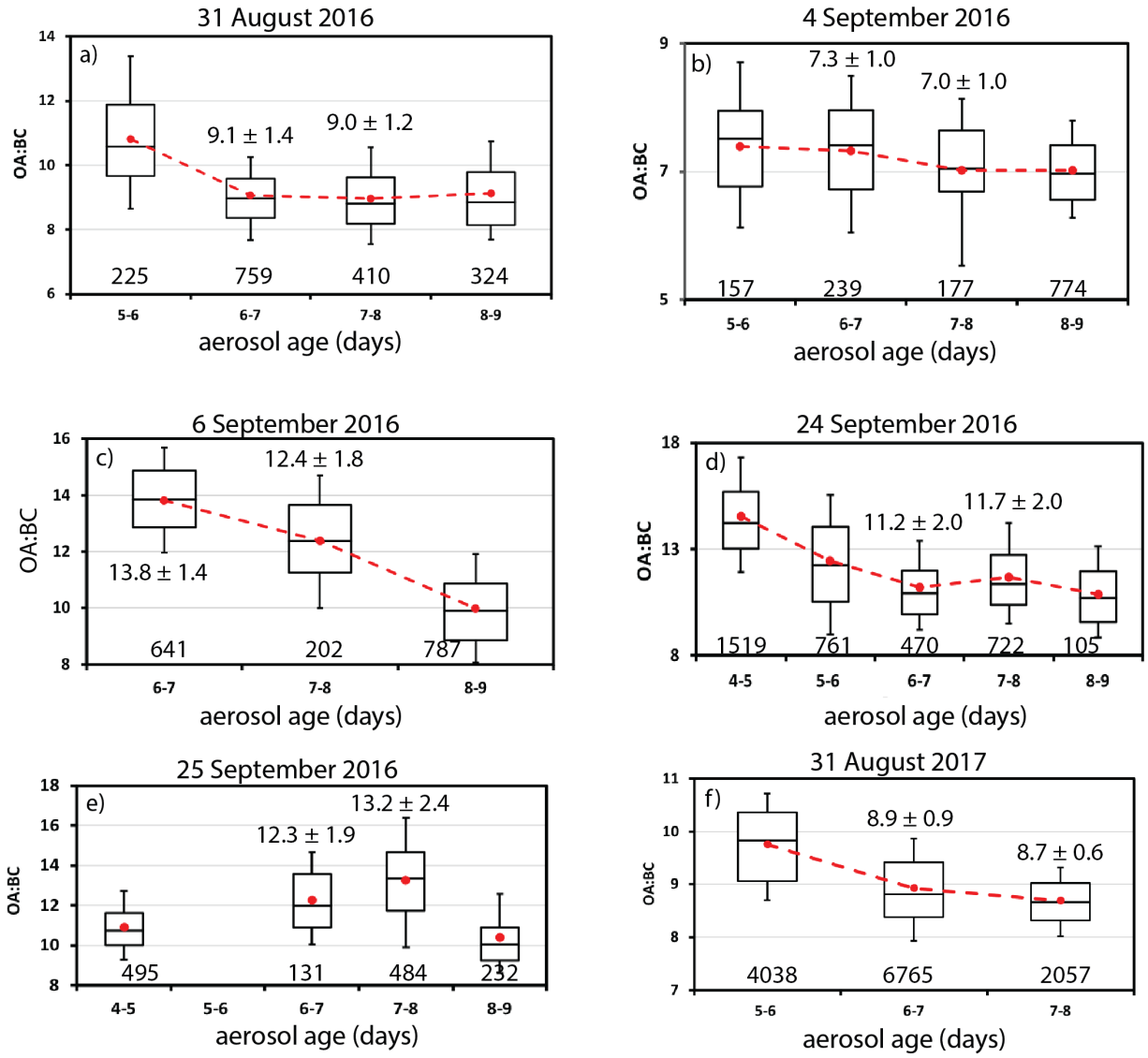

Supplementary Figure S8: OA:BC versus model-derived age for individual flights in September 2016 and 2017 flights for OA>20µg/m^3. Whiskers represent the 10th and 90th percentiles, boxes illustrate the 75th and 25th percentiles with a line indicating the median. The mean is represented by the red marker. Number of seconds of data within each age bin indicated above x-axis. Y-axis ranges vary for each flight.

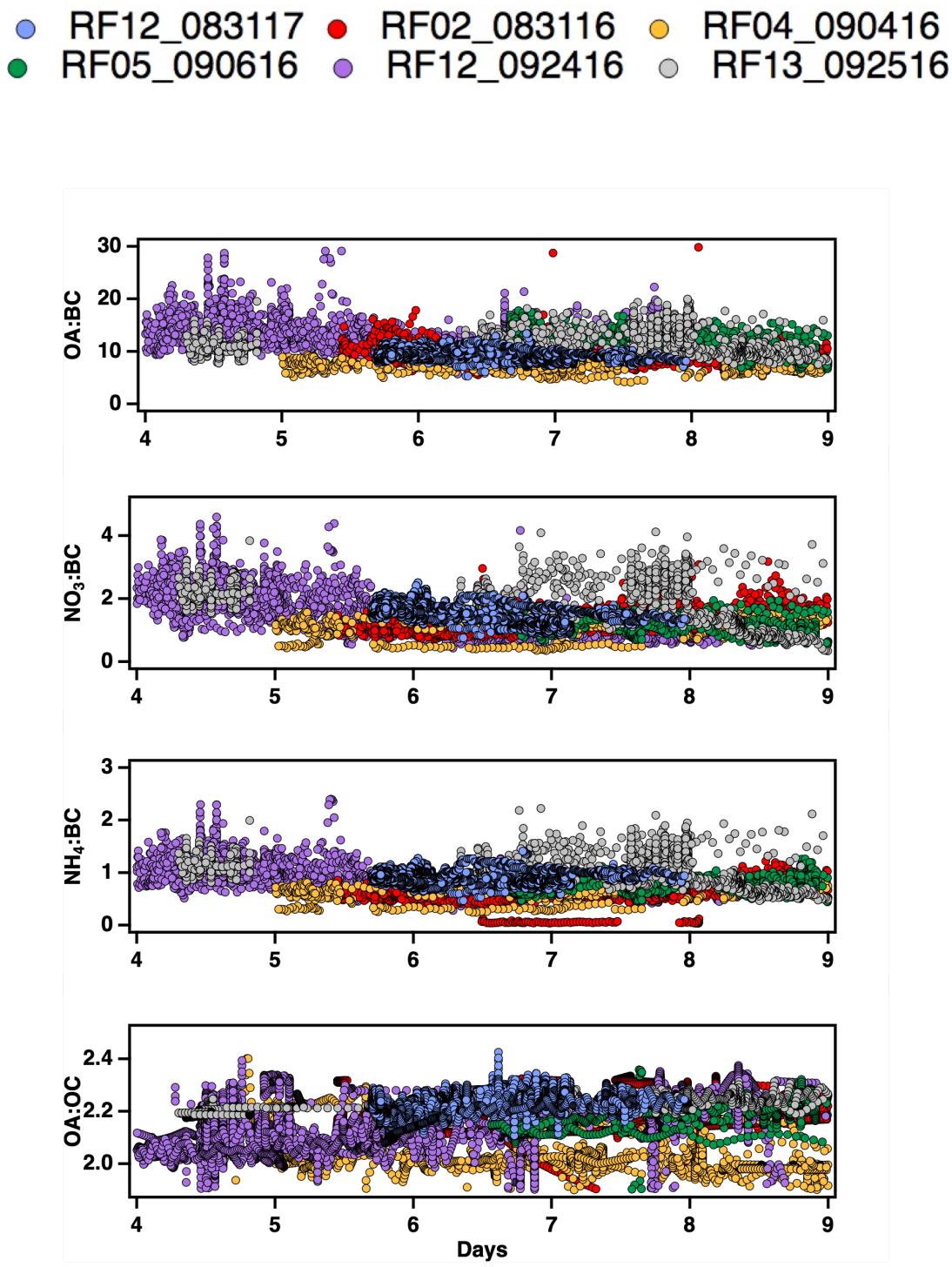

Supplementary Figure S9. The bulk species ratios with respect to model-derived time since emission colored by flight for top) OA:BC, 2nd panel) NO_3:BC, 3rd panel) NH_4:BC, 4th panel) SO_4:BC. OA:OC. OA>20 ug m^{-3} only.

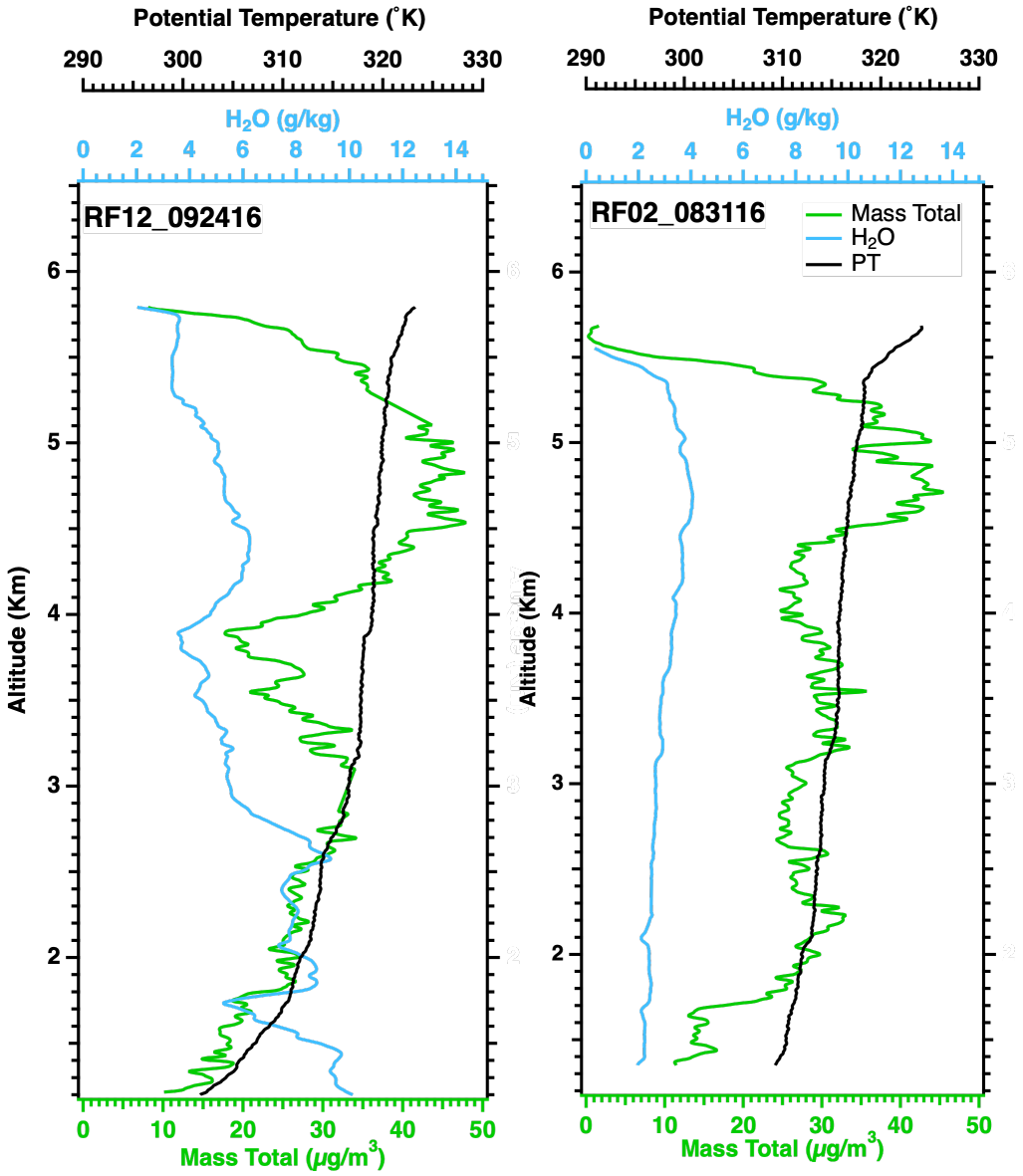

Supplementary Figure S10. Water vapor (blue), potential temperature (black), mass total concentration (OA+SO_4+NO_3+NH_4+BC) (green) vertical profiles for left) 24 September, 2016 (12.34^0 S, 11^0 E) and right) 31 August, 2016 (16^0 S, 5^0 E).

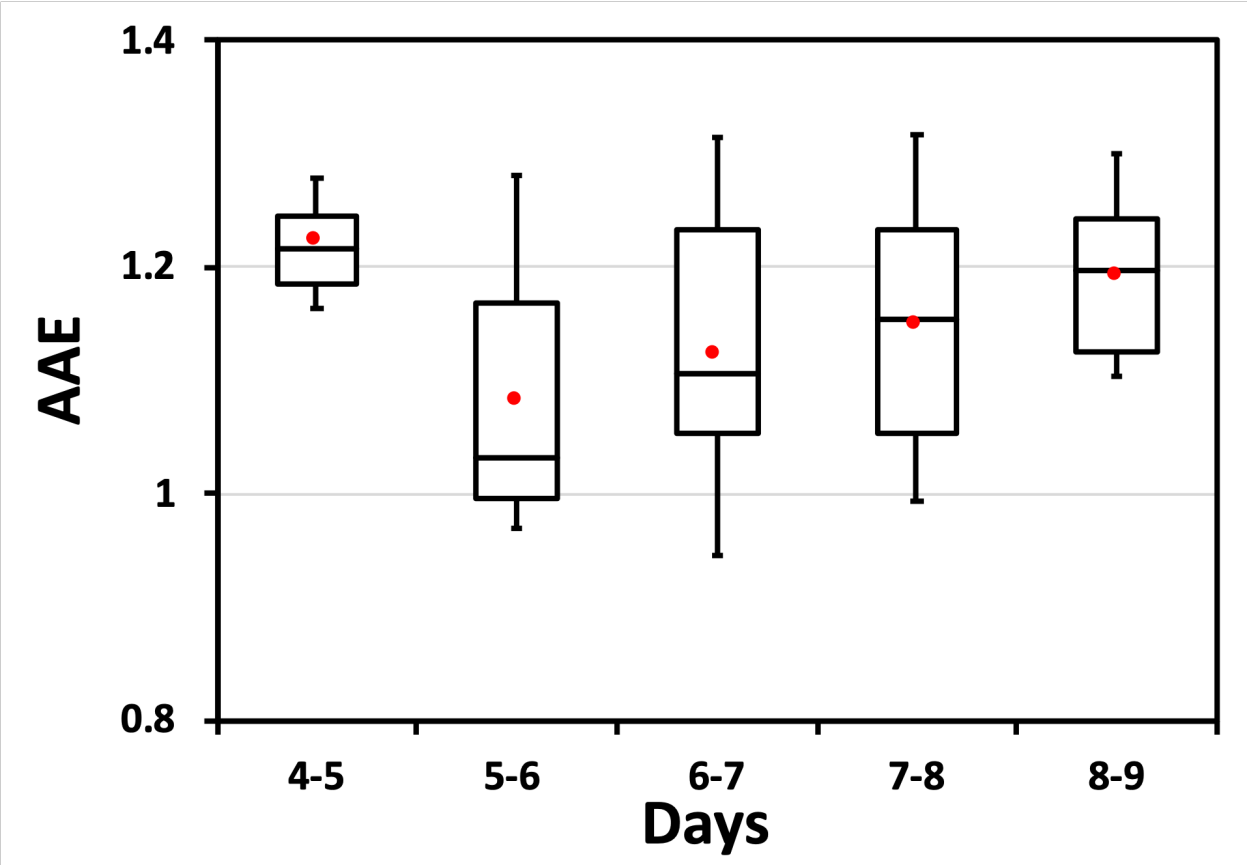

Supplementary Figure S11. Absorption Angstrom exponent (AAE) vs Age for selected flights where OA>20µg/m^3. Whiskers represent the 10th and 90th percentiles, boxes illustrate the 75th and 25th percentiles with a line indicating the median and the mean represented by the red filled circle.

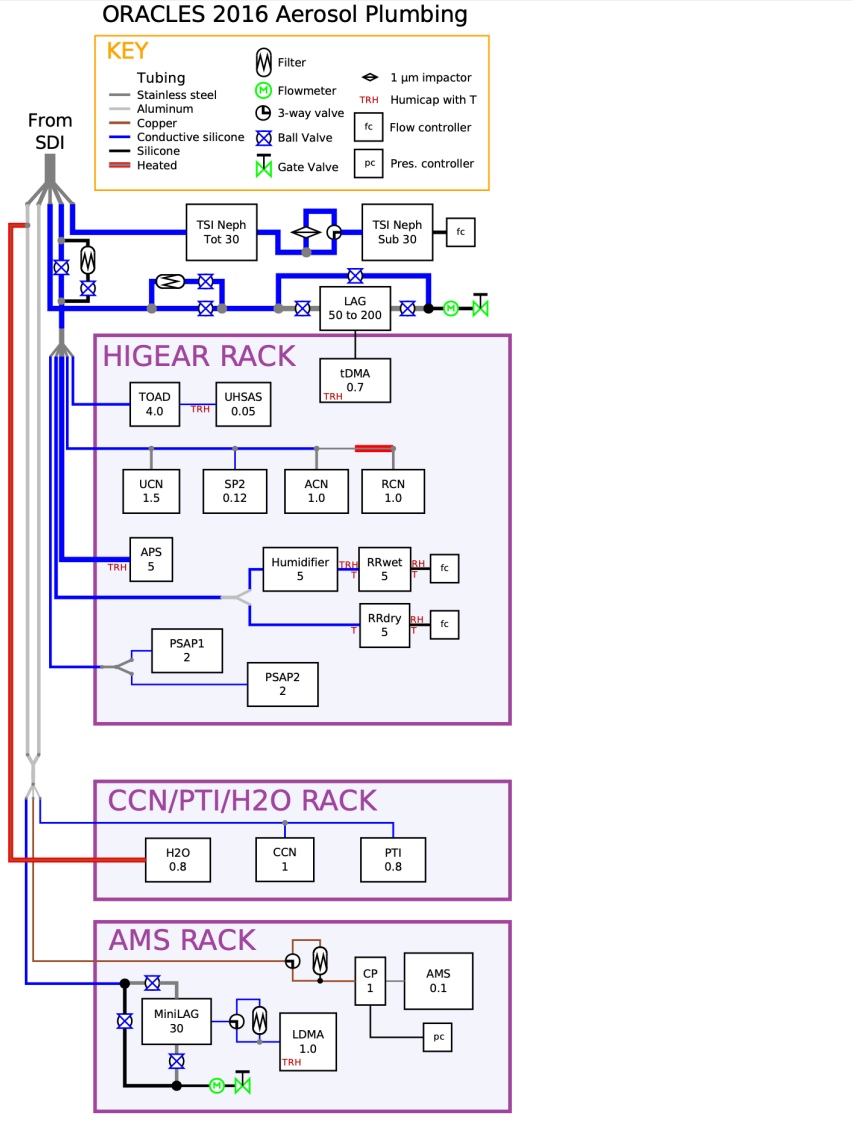

Supplementary Figure S12: Layout of aerosol instrumentation relative to the inlet for the 2016 campaign. The numbers below the instrument acronyms represent flow rates in lpm. Note the lag and mini-lag include a small leak included to equalize the pressure between the two. The line widths are proportional to the nominal diameter of the tubing (outer for metal, inner for silicone). Exceptions are the AMS, SP2, and UHSAS, which have very low flow rates and such tiny inlet tubes that they wouldn't be visible.

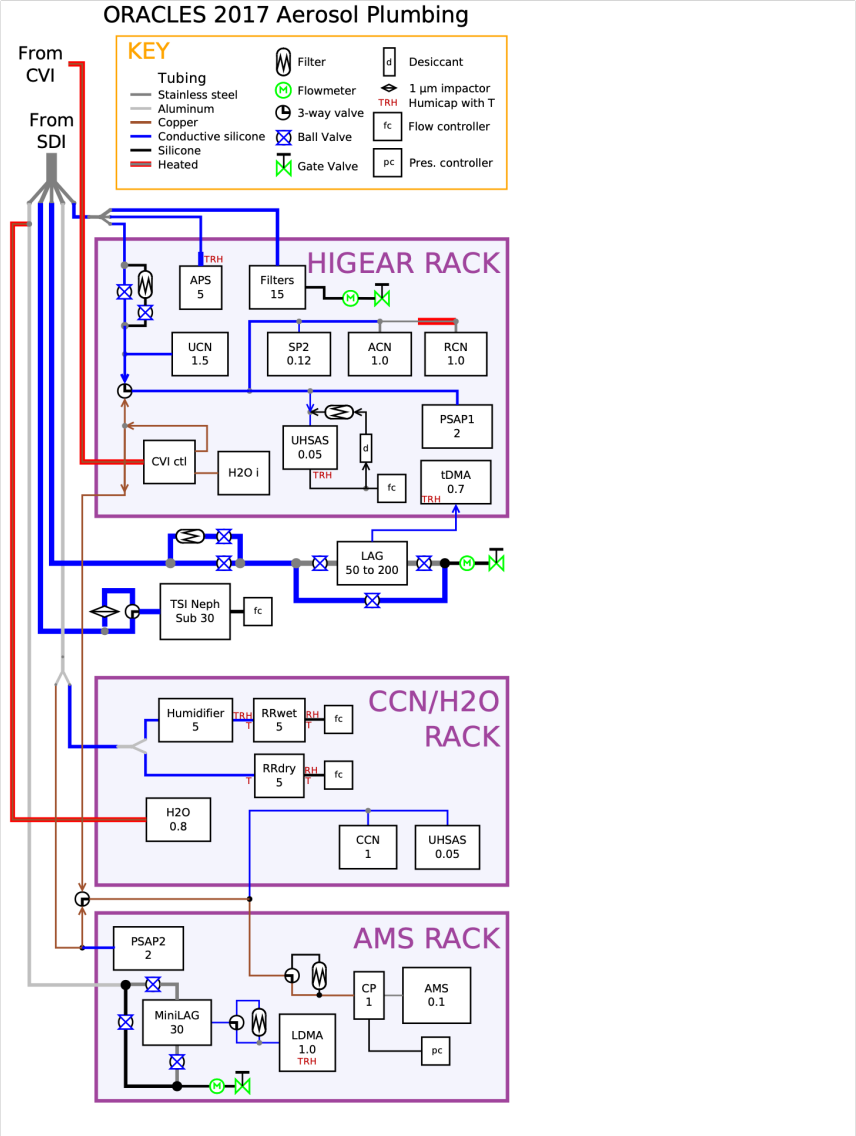

Supplementary Figure S13: Layout of aerosol instrumentation relative to the inlet for the August 31, 2017 flight. Most flow is down and to the right, the addition of a counter-flow virtual impactor inlet (CVI) modified some flow direction to be up and to the left; flow direction arrows are included in critical spots to aid understanding. Other comments on the diagram Fig. S10 for 2016 also apply here.

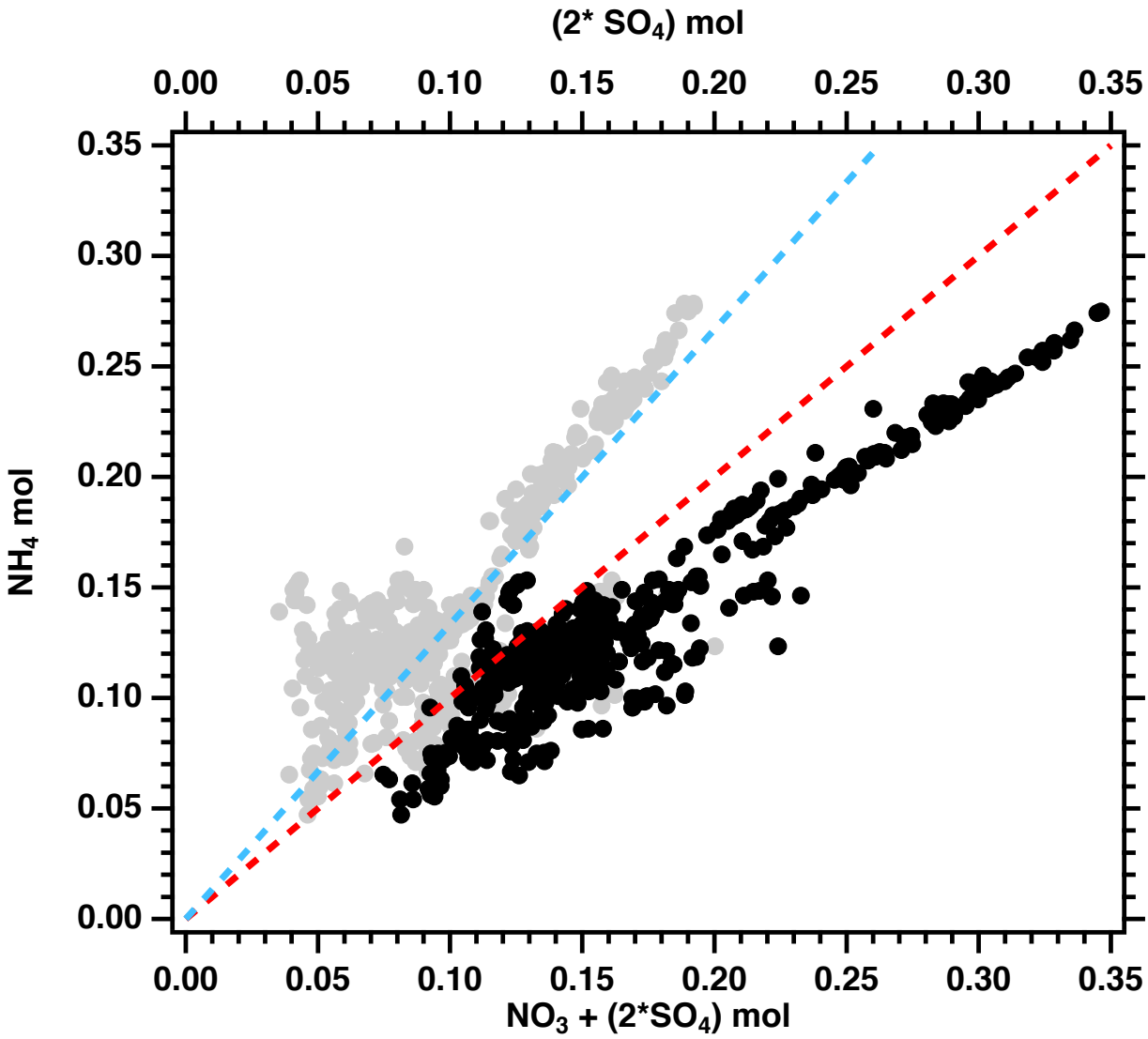

Supplementary Figure S14: Measured ammonium in moles as a function of the molar sum of nitrate and 2*sulphate for one-minute measurements from all 6 flights (1s average), constrained to the free troposphere. Values below the 1:1 line indicate aerosol that is acidic.